

## Excitonic condensation and metal-semiconductor transition in AA bilayer graphene in an external magnetic field

V. Apinyan<sup>1</sup>\* and T. K. Kopeć<sup>1</sup>

*Institute of Low Temperature and Structure Research, Polish Academy of Sciences, 50-422 Wrocław, ul. Okólna 2, Poland*



(Received 18 January 2022; revised 13 April 2022; accepted 18 April 2022; published 2 May 2022)

In this paper, the effects of the external transverse magnetic field  $B$  (perpendicular to the surface of the layers) on electronic and excitonic properties are studied in AA-stacked bilayer graphene (BLG). The effects of the Coulomb interactions and excitonic pairing have been taken into account and analyzed in detail within the bilayer Hubbard model. Both half-filling and partial-filling regimes have been taken into account and the magnetic field dependence of a series of physical parameters was found. It is shown that the difference between the average electron concentrations in the layers vanishes at some critical value of magnetic field  $B_c$  and the chemical potential is calculated numerically above and below that value. The role of the Coulomb interactions on the average carrier concentrations in the layers has been analyzed and the excitonic order parameters have been calculated for different spin orientations. We found a possibility for the particle population inversion between the layers when varying the external magnetic field. The calculated electronic band structure in AA-BLG shows the presence of a metal-semiconductor transition, governed by the strength of the applied magnetic field or the interlayer interaction potential. We show that for high magnetic fields, the band gap approaches the typical values of the gaps in the usual semiconductors. It is demonstrated that, at some parameter regimes, AA-BLG behaves like a spin-valve device by permitting the electron transport with only one spin direction. All calculations have been performed at the zero-temperature limit.

DOI: [10.1103/PhysRevB.105.184503](https://doi.org/10.1103/PhysRevB.105.184503)

### I. INTRODUCTION

Bilayer graphene (BLG) systems have been the subject of many theoretical and experimental investigations due to their interesting physical properties [1–8]. Recently, stable AA-BLG structures have been obtained experimentally, which are promising for technological applications [9–12]. The opening of the band gap in the single-particle excitation spectrum of AB-stacked BLG systems under the influence of the electric field classified the AB-BLG among the semiconducting materials with a controllable gap parameter, which opened opportunities for their technological applications [1–4]. Despite many efforts to observe such a gap in the single-particle excitation spectrum of AA-BLG, the band structure of this system has been found with no excitation gap [3,13] and with linear energy spectrum. Recently, a possible band-gap opening issue was reported in Ref. [14], where the authors evaluated the transmission and reflection probabilities in AA-BLG with the layers encapsulated in the dielectric. The band gap found in their research is about 40 meV and is caused by the induced mass terms via the dielectric medium. This value of the gap is slightly larger than the value of the band gap found in single-layer graphene when using the substrates of SiC or h-BN ( $E_g \sim 20$  meV) [15,16]. Another interesting band-gap opening is related to the effect of spin-orbit coupling (SOC) in graphene, which is indeed found to be very small ( $E_{SO} \sim 10$   $\mu$ eV) [17,18]. In a series of works, the authors

showed the opening of the very small band gaps when including the effects of SOC [17–20]. These results are promising, mostly for studying the spin-Hall states in AA-BLG systems [19].

Concerning the theoretical side of studies, many interesting works have studied the metal-insulator transition and band-gap opening (in the low- $U$  limit) in doped AA-BLG [21,22], the influence of antiferromagnetism on the physical properties in AA-BLG [23–26], the coexistence of the antiferromagnetic and excitonic insulator phases [23–25], the dynamical instabilities in AA-BLG [25], the optical plasmonic gap opening [27], etc. Recently, an electronic transport gap was demonstrated in Ref. [28], and the charge-carrier dependence on the spin relaxation time was analyzed. Moreover, BLG-based spin-valve devices have been proposed in this context. In Ref. [29], a very large band-gap opening has been shown in unbiased AA-BLG with variable interlayer separation distance  $c_0$ , starting from van der Waals-like distances with  $c_0 = 3.58$  Å to small separation distances, allowing the chemical bondings between the carbon atoms situated in different layers in the bilayer. A series of phase transitions have been found, from the semimetal to the wide band-gap semiconducting one, when passing from van der Waals to covalent bond regimes.

The effect of the magnetic field on the electronic and transport properties in AA-BLG has been studied in a series of theoretical works [30–41]. The magnetic field dependence of thermal properties in doped AA-BLG has been considered theoretically in Refs. [30,34], where the presence of both electron- and hole-type contributions in transport properties has been shown in AA-BLG. However, up to now, few works

\*v.apinyan@intibs.pl

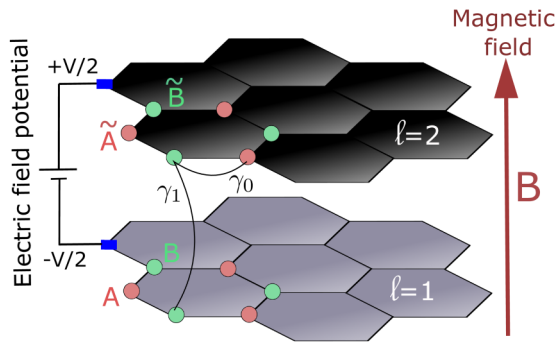


FIG. 1. The structure of biased AA-stacked bilayer graphene system with the applied external electric field potential  $V$  (with potential  $+V/2$  applied to the layer  $\ell = 2$  and  $-V/2$  at the bottom layer  $\ell = 1$ ) and transverse magnetic field  $B$  (see thick red-arrow in the picture), in the direction of the  $z$  axis. Different layers in the AA-BLG have been shown with two sublattice sites  $A, B$  in layer  $\ell = 1$  and  $\tilde{A}, \tilde{B}$  in layer  $\ell = 2$ .

have paid attention to the influence of the magnetic field on the charge redistribution and band-gap opening in pristine AA-BLG.

In this paper, we consider the effects of the magnetic field on the excitonic properties in the system and we show the possibilities of the excitonic condensates states in AA-BLG at different values of the magnetic field. We show the possibility of formation of different direct band gaps in the energy spectrum of AA-BLG under the influence of the transverse magnetic field (see Fig. 1). First, we show the existence of a critical value of the magnetic field above which the physical parameters in the system change their behavior. We show theoretically that the complete charge neutrality (CN) (when the average total charge densities in both layers get equal values) could be achieved at the half-filling case and the average electron population inversion occurs only in the case of partial filling. The CN in the AA-BLG system could be also obtained when varying the interlayer interaction potential. This effect is also discussed in the present paper. The CN of the entire BLG system is important for its nondestructive applications in modern technological devices. To achieve the CN in such construction, a huge number of internal and external physical parameters should be properly considered and tuned [37]. This also requires an important experimental setup and effort to calibrate the BLG system at the CN [38]. The electronic and transport properties at the CN and away from it have been discussed in a number of works [42–47].

Furthermore, we calculate the band gaps in the system and how that they are spin dependent and totally controllable by the strength of the applied magnetic field. Our numerical calculations demonstrate that the opened band gaps are comparable with the band gaps in typical direct low-band-gap semiconducting systems of types  $A^{\text{III}}B^{\text{V}}$  or  $A^{\text{IV}}B^{\text{VI}}$  [48]. Particularly, we show that in the regime of noninteracting layers (and in the presence of the magnetic field), a very large band gap opens in the electronic band structure with the value of the band gap  $E_g \sim 200$  meV (much larger than those obtained from SOC considerations [17–20]), The transition from semiconducting to weak-metallic states occurs when in-

creasing the interlayer Coulomb potential. Meanwhile, when varying the magnetic field, from zero up to high values, an opposite transition occurs (at half filling), from the metallic to the semiconducting state with a sufficiently large band gap of order  $E_g \sim 150.6$  meV, typical for semiconducting systems of types  $A^{\text{III}}B^{\text{V}}$  or  $A^{\text{IV}}B^{\text{VI}}$  [48]. Our results suggest that, for the given range of parameters and conditions imposed on the system, one can quench the electronic conductivity in one spin channel (for example,  $\sigma = \uparrow$ ), while the other one ( $\sigma = \downarrow$ ) remains open. Those results are purposeful for the use of AA-BLG as the spin-valve device [49,50], for examining the spin-controlled quantum transport at the nanoscale [51–56] and excitonic condensation phenomena, not observed yet experimentally [57–59].

The present paper is organized as follows: In Sec. II, we introduce the AA BLG within the generalized Hubbard model. In Sec. III, we obtain the electronic band structure and we give the set of self-consistent (SC) equations. In Sec. IV, we present the numerical results for the important physical quantities in the system we discuss different band-gap formations. In Sec. V, we give a conclusion to our paper. In Appendix A, we obtain the system of SC equations and in Appendix B the mean-field decouplings procedures are discussed.

## II. HAMILTONIAN OF THE INTERACTING AA-BLG

### A. Bilayer Hubbard Hamiltonian with magnetic field

We consider here the BLG structure composed of two layers, and each atom in the top layer is stacked on top of a similar atom in the bottom layer. Moreover, there is no shift in their local atomic space position  $\mathbf{r}$ . This type of stacking order is called AA stacking. The Hamiltonian of the AA-BLG in the presence of the external static electric field-potential  $V$  and magnetic field  $\mathbf{B}$  (oriented along the  $z$  axis, perpendicular to the planes of the layers) could be written in the following form:

$$\hat{H}_{\text{AA}} = \hat{H}_{\gamma_0} + \hat{H}_{\gamma_1} + \hat{H}_U + \hat{H}_W + \hat{H}_V + \hat{H}_{\text{int}} + \hat{H}_{\mu}, \quad (1)$$

where

$$\begin{aligned} \hat{H}_{\gamma_0} = & -\gamma_0 \sum_{\langle \mathbf{r}, \mathbf{r}' \rangle} \sum_{\sigma} (\hat{a}_{\sigma}^{\dagger}(\mathbf{r}) \hat{b}_{\sigma}(\mathbf{r}') + \text{H.c.}) \\ & - \gamma_0 \sum_{\langle \mathbf{r}, \mathbf{r}' \rangle} \sum_{\sigma} (\hat{\tilde{a}}_{\sigma}^{\dagger}(\mathbf{r}) \hat{\tilde{b}}_{\sigma}(\mathbf{r}') + \text{H.c.}) \end{aligned} \quad (2)$$

is the intralayer electron hopping Hamiltonian and the interlayer hopping term is given by the Hamiltonian

$$\hat{H}_{\gamma_1} = -\gamma_1 \sum_{\mathbf{r}\sigma} (\hat{a}_{\sigma}^{\dagger}(\mathbf{r}) \hat{\tilde{a}}_{\sigma}(\mathbf{r}) + \hat{b}_{\sigma}^{\dagger}(\mathbf{r}) \hat{\tilde{b}}_{\sigma}(\mathbf{r}) + \text{H.c.}). \quad (3)$$

The operators  $\hat{a}_{\sigma}(\mathbf{r})$ ,  $\hat{b}_{\sigma}(\mathbf{r})$ ,  $\hat{\tilde{a}}_{\sigma}(\mathbf{r})$ , and  $\hat{\tilde{b}}_{\sigma}(\mathbf{r})$  describe the destruction of electrons at the given lattice site positions and the operators  $\hat{a}_{\sigma}^{\dagger}(\mathbf{r})$ ,  $\hat{b}_{\sigma}^{\dagger}(\mathbf{r})$ ,  $\hat{\tilde{a}}_{\sigma}^{\dagger}(\mathbf{r})$ ,  $\hat{\tilde{b}}_{\sigma}^{\dagger}(\mathbf{r})$  are the electron creation operators. The index  $\sigma$  denotes the spin variable, which takes two possible directions:  $\sigma = \uparrow$  or  $\sigma = \downarrow$ . The electrons enter into covalent bonds in the graphene's layers and are attached with the atoms near atomic sites  $A, B$  (in the layer with  $\ell = 1$ ) and  $\tilde{A}, \tilde{B}$  (in the layer with  $\ell = 2$ ) (see the picture in Fig. 1). The parameter  $\gamma_0$  is the energy necessary for the hopping of

electrons between the adjacent lattice sites in the layers. The summations  $\langle \dots \rangle$  in Eq. (2) are taken over the nearest-neighbor lattice site positions  $\mathbf{r}, \mathbf{r}'$  in the separate graphene layers. The energy parameter  $\gamma_1$ , in Eq. (3), describes the local hopping of electrons between adjacent layers  $\ell = 1$  and  $\ell = 2$ . The values, found experimentally, for the hopping parameters are  $\gamma_0 \sim 3$  eV and  $\gamma_1 = 0.257$  eV, as reported in Ref. [60]. Next, the summations in Eq. (3) are over the lattice sites positions  $\mathbf{r} = 1, 2, \dots, N$  and the electron spin configurations with  $\sigma = \uparrow, \downarrow$ . The Coulomb interaction terms  $\hat{\mathcal{H}}_U$  and  $\hat{\mathcal{H}}_W$  are given as

$$\hat{\mathcal{H}}_U = U \sum_{\mathbf{r}\eta} \hat{n}_{\eta\uparrow}(\mathbf{r})\hat{n}_{\eta\downarrow}(\mathbf{r}) \quad (4)$$

and

$$\hat{\mathcal{H}}_W = W \sum_{\mathbf{r}\sigma\sigma'} \hat{n}_{a\sigma}(\mathbf{r})\hat{n}_{\bar{a}\sigma'}(\mathbf{r}) + W \sum_{\mathbf{r}\sigma\sigma'} \hat{n}_{b\sigma}(\mathbf{r})\hat{n}_{\bar{b}\sigma'}(\mathbf{r}), \quad (5)$$

where  $U$  in Eq. (4) is the on-site Coulomb repulsion between the electrons in the layers  $\ell = 1, 2$ . We suppose that the value of it is uniform in both layers. The second summation in Eq. (4) is over all sublattice variables  $\eta = a, b, \bar{a}, \bar{b}$ . The parameter  $W$  in Eq. (5) denotes the local interlayer Coulomb interaction between the electrons at the same sublattice sites  $A, \bar{A}$  and  $B, \bar{B}$  in different layers. The operators  $\hat{n}_{\eta\uparrow}(\mathbf{r})$  and  $\hat{n}_{\eta\downarrow}(\mathbf{r})$  in Eq. (4) are the electron density operators for  $\sigma = \uparrow$  and  $\sigma = \downarrow$  and they are given as

$$\hat{n}_{\eta\sigma}(\mathbf{r}) = \hat{\eta}_\sigma^\dagger(\mathbf{r})\hat{\eta}_\sigma(\mathbf{r}). \quad (6)$$

The Coulomb potential  $W$ , in Eq. (5), is coupled to the product of particle density operators  $\hat{n}_{\eta\sigma}$  and  $\hat{n}_{\bar{\eta}\sigma'}$  in different layers (with  $\eta \neq \bar{\eta}$  and  $\sigma, \sigma' = \uparrow\downarrow$ ), defined in Eq. (6).

Next, the couplings with the external electric potential and magnetic fields are given by the terms  $\hat{\mathcal{H}}_V$  and  $\hat{\mathcal{H}}_{\text{int}}$  in Eq. (1). We have

$$\hat{\mathcal{H}}_V = \frac{V}{2} \sum_{\mathbf{r}} (\hat{n}_2(\mathbf{r}) - \hat{n}_1(\mathbf{r})), \quad (7)$$

where  $V$  is the electric field potential with the value  $+V/2$  at the top layer  $\ell = 2$  and the value  $-V/2$  at the bottom layer  $\ell = 1$  (see Fig. 1). The operators  $\hat{n}_1(\mathbf{r})$  and  $\hat{n}_2(\mathbf{r})$  in Eq. (7) are total density operators in the individual layers, i.e.,

$$\begin{aligned} \hat{n}_1(\mathbf{r}) &= \hat{n}_a(\mathbf{r}) + \hat{n}_b(\mathbf{r}), \\ \hat{n}_2(\mathbf{r}) &= \hat{n}_{\bar{a}}(\mathbf{r}) + \hat{n}_{\bar{b}}(\mathbf{r}). \end{aligned} \quad (8)$$

In turn, the operators  $\hat{n}_\eta(\mathbf{r})$ , on the right-hand sides of Eqs. (8) are given in the form

$$\hat{n}_\eta(\mathbf{r}) = \sum_{\sigma} \hat{n}_{\eta\sigma}(\mathbf{r}). \quad (9)$$

Furthermore, the coupling with the magnetic field is given as

$$\hat{\mathcal{H}}_{\text{int}} = -g\mu_B B_z \sum_{\mathbf{r}\eta} (\hat{n}_{\eta\uparrow} - \hat{n}_{\eta\downarrow}). \quad (10)$$

The parameter  $g$  in Eq. (10) is the Landé  $g$ -factor and its value can be derived naturally from Dirac's equation ( $g \sim 2$ , according to recent experimental measurements of this physical parameter in graphene structures [61]). Next,  $\mu_B$ , in

Eq. (10), is the Bohr magneton [62] (intrinsic magnetic moment of an electron), which we put equal to 1 (here, we use the convention  $\hbar = 1$ ) throughout this paper. We consider here the magnetic field in the  $z$  direction, perpendicular to the layers in the AA-BLG (see the thick-red arrow in Fig. 1). The Hamiltonian  $\hat{\mathcal{H}}_\mu$ , in Eq. (1), is the chemical potential term and is given as

$$\hat{H}_\mu = -\mu \sum_{\mathbf{r}} \hat{n}(\mathbf{r}). \quad (11)$$

We ignored in Eq. (1) the spin-orbit coupling due to the fact that the effect on the band-gap, resulting from this type of interaction, is very small [17–19].

Furthermore, we introduce the fermionic Grassmann complex variables at the place of usual electron operators and write the expression of the partition function of the system in terms of the Grassmann field variables (see a similar description in Ref. [63]). We write the partition function  $\mathcal{Z}$  of the AA-BLG system in the formalism based on the fermionic path integrals (see, in Refs. [63,64]),

$$\mathcal{Z} = \text{Tr} e^{-\beta\mathcal{H}} = \int \prod_{\eta} [D\bar{\eta}D\eta] e^{-\mathcal{S}}, \quad (12)$$

where  $\mathcal{H}$  is the total Hamiltonian of the AA-BLG and parameter  $\beta$ , in the exponential, in Eq. (12), is given after the imaginary-time Matsubara formalism (with  $0 < \tau < \beta$ ) [65], and we have  $\beta = 1/T$ , where  $T$  is the thermodynamic temperature. Here, we used the units where the Boltzmann is  $k_B = 1$ .

Furthermore, we note  $\mathcal{S} = \mathcal{S}[\bar{a}, a, \bar{b}, b, \bar{\bar{a}}, \bar{\bar{a}}, \bar{\bar{b}}, \bar{\bar{b}}]$  as the total fermionic action of the system in terms of Grassmann variables. It is given in the imaginary time Matsubara representation. It can be expressed with the help of total Hamiltonian  $\mathcal{H}_{\mathcal{A}\mathcal{A}}(\tau)$  as

$$\mathcal{S} = \int_0^\beta d\tau \mathcal{H}_{\mathcal{A}\mathcal{A}}(\tau) + \sum_{\eta} \mathcal{S}_B[\bar{\eta}, \eta]. \quad (13)$$

Next,  $\mathcal{S}_B[\bar{\eta}, \eta]$ , are the electronic Berry terms [66] and they are given by

$$\mathcal{S}_B[\bar{\eta}, \eta] = \sum_{\mathbf{r}\sigma} \int_0^\beta d\tau \bar{\eta}_\sigma(\mathbf{r}\tau) \partial_\tau \eta_\sigma(\mathbf{r}\tau). \quad (14)$$

## B. Linearization of the quadratic density terms

In fact, the nonlinear density terms, figuring in the Hubbard interaction Hamiltonians, in Eqs. (4) and (5) could be decoupled with the help of a series of Hubbard-Stratanovich (HS) transformations, which are indeed equivalent to the usual mean-field approximations. A detailed description of such procedures is given in Appendix B. Here, we present only the resulting contributions to the total Hamiltonian and action of the BLG system coming from such decouplings. First, the contribution from the linearization procedure of the Coulomb- $U$  term in Eq. (4) is following

$$\delta\mathcal{S}_U = - \sum_{\mathbf{r}\eta} \int_0^\beta d\tau \frac{U}{2} \bar{n}_\eta n_\eta(\mathbf{r}\tau) \quad (15)$$

and the contribution to the total Hamiltonian in Eq. (1) is straightforward:

$$\delta\mathcal{H}_U = \frac{U}{2} \sum_{\mathbf{r}\eta} \bar{n}_\eta n_\eta(\mathbf{r}\tau). \quad (16)$$

Here, the notation  $\bar{n}_\eta$  means the grand canonical average of the density function  $n_\eta(\mathbf{r}\tau)$ , i.e., in usual writing, we have  $\bar{n}_\eta = \langle n_\eta \rangle$ . It could be calculated exactly with the help of the partition function, in Eq. (12), as

$$\langle \dots \rangle = \frac{1}{\mathcal{Z}} \int \prod_{\eta} [D\bar{\eta}D\eta] \dots e^{-\mathcal{S}}. \quad (17)$$

When deriving the result in Eq. (16), we have supposed that the average densities, corresponding to opposite spin orientations, are equal:  $\langle n_{\eta\uparrow}(\mathbf{r}\tau) \rangle = \langle n_{\eta\downarrow}(\mathbf{r}\tau) \rangle$ . Next, the contributions coming from the decouplings of the interlayer Coulomb interaction terms in Eq. (6) have been obtained in the forms

$$\delta\mathcal{S}_W = - \sum_{\mathbf{r}\sigma} \sum_{\lambda} \int_0^{\beta} d\tau \Delta_{\sigma}^{(\lambda)} \lambda_{\sigma}^{\dagger}(\mathbf{r}\tau) \tilde{\lambda}_{\sigma}(\mathbf{r}\tau) \quad (18)$$

and

$$\delta\mathcal{H}_W = - \sum_{\mathbf{r}\sigma} \sum_{\lambda} \Delta_{\sigma}^{(\lambda)} \lambda_{\sigma}^{\dagger}(\mathbf{r}\tau) \tilde{\lambda}_{\sigma}(\mathbf{r}\tau), \quad (19)$$

where the summation index  $\lambda$  takes two values  $a$  and  $b$  and  $\Delta_{\sigma}^{(\lambda)}$  is the interlayer excitonic order parameter corresponding to the formation of the excitons between the electrons and holes at the sublattice site positions  $A-\tilde{A}$  or  $B-\tilde{B}$ , which define the summation parameter  $\lambda$ . We have

$$\Delta_{\sigma}^{(\lambda)} = W \langle \lambda_{\sigma}^{\dagger}(\mathbf{r}\tau) \tilde{\lambda}_{\sigma}(\mathbf{r}\tau) \rangle. \quad (20)$$

Then the total Hamiltonian in Eq. (1) could be rewritten in the form which is linear in fermionic densities. In Grassmann variable notations, we have

$$\mathcal{H}_{AA} = \mathcal{H}_{\gamma_0} + \mathcal{H}_{\gamma_1} + \delta\mathcal{H}_U + \delta\mathcal{H}_W + \mathcal{H}_V + \mathcal{H}_{\text{int}} + \mathcal{H}_{\mu}. \quad (21)$$

In the next section, we will use this form of the Hamiltonian for writing the expression of the inverse Green's function matrix of the considered system and to derive the set of SC equations.

### III. THE PARTICLE EXCITATION QUASIENERGIES

#### A. The inverse Green's function and electronic band structure

In the following sections, we will use total fermionic action, written in Eq. (13), to calculate the Green's functions matrices and to derive the single quasiparticle excitation quasienergies which form the electronic band structure in the AA-BLG system. We will pass into the reciprocal space representation for the creation and annihilation operators  $\bar{\eta}_{\sigma}(\mathbf{r}\tau)$  and  $\eta_{\sigma}(\mathbf{r}\tau)$ . For this, we perform the Fourier transformation into the reciprocal space representation ( $\mathbf{k}$ ,  $\nu_n$ ),

$$\eta_{\sigma}(\mathbf{r}\tau) = \frac{1}{\beta N} \sum_{\mathbf{k}\nu_n} \eta_{\sigma}(\mathbf{k}\nu_n) e^{i(\mathbf{k}\mathbf{r} - \nu_n\tau)}, \quad (22)$$

where  $N$  is the number of the reciprocal lattice points and the summation on the right-hand side of Eq. (22) is over the reciprocal wave vectors  $\mathbf{k}$  and fermionic Matsubara frequencies  $\nu_n$  with  $\nu_n = \frac{\pi}{\beta}(2n+1)$  [65], where  $n$  is an integer number (i.e.,  $n = 0, \pm 1, \pm 2, \dots$ ). Next, we introduce the Nambu spinors [63]  $\tilde{\Psi}_{\sigma}(\mathbf{k}\nu_n)$  and  $\Psi_{\sigma}(\mathbf{k}\nu_n)$  for the considered problem. We have

$$\Psi_{\sigma}(\mathbf{k}\nu_n) = \begin{pmatrix} a_{\sigma}(\mathbf{k}\nu_n) \\ b_{\sigma}(\mathbf{k}\nu_n) \\ \tilde{a}_{\sigma}(\mathbf{k}\nu_n) \\ \tilde{b}_{\sigma}(\mathbf{k}\nu_n) \end{pmatrix} \quad (23)$$

and

$$\tilde{\Psi}_{\sigma}(\mathbf{k}\nu_n) = (\tilde{a}_{\sigma}(\mathbf{k}\nu_n), \tilde{b}_{\sigma}(\mathbf{k}\nu_n), \bar{a}_{\sigma}(\mathbf{k}\nu_n), \bar{b}_{\sigma}(\mathbf{k}\nu_n)). \quad (24)$$

Then, the total fermionic action could be written in the Fourier transformed form:

$$\mathcal{S}[\tilde{\Psi}, \Psi] = \frac{1}{\beta N} \sum_{\mathbf{k}\nu_n} \sum_{\sigma} \tilde{\Psi}_{\sigma}(\mathbf{k}\nu_n) \mathcal{G}_{\sigma}^{-1}(\mathbf{k}\nu_n) \Psi_{\sigma}(\mathbf{k}\nu_n). \quad (25)$$

Indeed, the forms of the inverse Green's functions, corresponding to the opposite spin directions, are different as we will see later on. In other words, the total action of the system becomes composed of two parts  $\mathcal{S}[\tilde{\Psi}, \Psi] = \mathcal{S}_{\uparrow}[\tilde{\Psi}, \Psi] + \mathcal{S}_{\downarrow}[\tilde{\Psi}, \Psi]$ . For the matrices  $\mathcal{G}_{\uparrow}^{-1}(\mathbf{k}\nu_n)$  and  $\mathcal{G}_{\downarrow}^{-1}(\mathbf{k}\nu_n)$ , we get the following analytical expressions:

$$\mathcal{G}_{\sigma}^{-1}(\mathbf{k}\nu_n) = \begin{pmatrix} E_{1\sigma}(\nu_n) & -\tilde{\gamma}_{0\mathbf{k}} & -(\gamma_1 + \Delta_{\sigma}) & 0 \\ -\tilde{\gamma}_{0\mathbf{k}}^* & E_{1\sigma}(\nu_n) & 0 & -(\gamma_1 + \Delta_{\sigma}) \\ -(\gamma_1 + \Delta_{\sigma}) & 0 & E_{2\sigma}(\nu_n) & -\tilde{\gamma}_{0\mathbf{k}} \\ 0 & -(\gamma_1 + \Delta_{\sigma}) & -\tilde{\gamma}_{0\mathbf{k}}^* & E_{2\sigma}(\nu_n) \end{pmatrix}. \quad (26)$$

The diagonal elements  $E_{i\sigma}(\nu_n)$  (with  $i = 1, 2$ ) in the matrices Eq. (26) represent the shifted single-particle quasienergies and are given by the following expressions:

$$E_{i\sigma}(\nu_n) = -i\nu_n - (-1)^i \frac{V}{2} + x_{i\sigma}. \quad (27)$$

In turn, the interaction-normalized parameters  $x_{i\sigma}$ , in Eq. (27) are given via the expressions

$$\begin{aligned} x_{1\sigma} &= 2W - \mu + (-1)^{\sigma} g\gamma_0 \tilde{B} + \frac{U}{2} \bar{n}_a, \\ x_{2\sigma} &= -\mu + (-1)^{\sigma} g\gamma_0 \tilde{B} + \frac{U}{2} \bar{n}_{\tilde{a}}, \end{aligned} \quad (28)$$

where

$$(-1)^\sigma = \begin{cases} +1, & \text{if } \sigma = \uparrow \\ -1, & \text{if } \sigma = \downarrow. \end{cases} \quad (29)$$

Here, we have put  $\tilde{B} \equiv \mu_B B / \gamma_0$  and the averages  $\bar{n}_a$  and  $\bar{n}_{\tilde{a}}$  signify the spin-summed average fermionic densities at the lattice sites in sublattices  $A$  and  $\tilde{A}$  (see Fig. 1). Next, the parameters  $\tilde{\gamma}_{0\mathbf{k}}$  are renormalized hopping amplitudes:

$$\tilde{\gamma}_{0\mathbf{k}} = \gamma_0 \sum_{\delta} e^{-i\mathbf{k}\delta}. \quad (30)$$

The vectors  $\delta$ , in Eq. (30), represent the nearest-neighbor vectors in different layers  $\ell = 1, 2$ . The components of  $\delta$  are the same for  $\ell = 1, 2$  ( $\delta_i^{\ell=1} = \delta_i^{\ell=2} \equiv \delta_i$  with  $i = 1, \dots, 3$ ) and are given by

$$\delta = \begin{cases} \delta_1 = \left(\frac{a}{2\sqrt{3}}, \frac{a}{2}\right) \\ \delta_2 = \left(\frac{a}{2\sqrt{3}}, -\frac{a}{2}\right) \\ \delta_3 = \left(-\frac{a}{\sqrt{3}}, 0\right), \end{cases} \quad (31)$$

where  $a = \sqrt{3}a_0$  in Eq. (31) is the sublattice constant, while  $a_0$  is the carbon-carbon length in the graphene layers (with  $a_0 = 1.42 \text{ \AA}$ ). Furthermore, the expressions of spin-dependent coefficients  $x_{i\sigma}$  in Eqs. (28) could be written with the help of the inverse filling coefficient  $\kappa$  and average charge density difference  $\delta\bar{n}$  between the layers. For sublattices  $A$  and  $\tilde{A}$  in the AA-BLG (see Fig. 1), these parameters could be defined in the following form:

$$\begin{aligned} \bar{n}_a + \bar{n}_{\tilde{a}} &= \frac{1}{\kappa}, \\ \bar{n}_{\tilde{a}} - \bar{n}_a &= \frac{\delta\bar{n}}{2}. \end{aligned} \quad (32)$$

Here, the coefficient  $\kappa$  describes the inverse of the total number of particles at the given lattice site position. It can be

expressed with the help of the filling coefficient  $n_{\text{fill}}$ , i.e.,  $\kappa = 1/n_{\text{fill}}$ . The maximum number of parameter  $\kappa$  is equal to 0.25, which corresponds to the fully filled lattice sites. If  $\kappa = 0.25$ , then we have the maximum average total number of particles in both layers (at the same given lattice site  $\mathbf{r}$  in both layers) equal to 4, according to the Pauli principle. If  $\kappa = 0.5$ , then we have the half-filling case with  $n_{\text{fill}} = 2$ . In the latter case, we have only one particle per sublattice site corresponding to the fermions of type  $a$  and  $\tilde{a}$ . The number  $\delta\bar{n}$  signifies the average charge density imbalance between the layers and is defined as

$$\delta\bar{n} = \bar{n}_2 - \bar{n}_1, \quad (33)$$

where the average charge densities  $\bar{n}_l$  (with the layers indices  $l = 1, 2$ ) mean the total average fermionic charge densities in the separate layers in the AA-BLG. Similar expressions could also be written for the sublattice charge densities  $\bar{n}_b$  and  $\bar{n}_{\tilde{b}}$  attached to lattice sites  $B$  and  $\tilde{B}$ , respectively. The average charge densities  $\bar{n}_a$  and  $\bar{n}_{\tilde{a}}$  could be expressed as

$$\begin{aligned} \bar{n}_a &= \frac{1}{2} \left( \frac{1}{\kappa} - \frac{\delta\bar{n}}{2} \right), \\ \bar{n}_{\tilde{a}} &= \frac{1}{2} \left( \frac{1}{\kappa} + \frac{\delta\bar{n}}{2} \right). \end{aligned} \quad (34)$$

Then we present the calculations results for the total single-particle quasienergies in AA-BLG, corresponding to different spin-directions. Those quasienergies define the electronic band structure in AA-BLG in various interactions regimes and are the subject for further consideration in the present paper. As mentioned earlier, we consider two different spin configurations in the system, i.e.,  $\sigma = \uparrow$ ,  $\sigma = \downarrow$ , and corresponding secular determinants  $\det \mathcal{G}_\sigma^{-1}(\mathbf{k}v_n)$ . The eigenvalues of the inverse Green's function matrices (for two different spin directions) could be obtained by solving the equations for secular determinants  $\det \mathcal{G}_\sigma^{-1}(\mathbf{k}v_n) = 0$ . The solutions of those equations give the exact band structure in the AA-BLG with excitonic correlations and interaction effects considered here. For the given spin  $\sigma$ , we have

$$\epsilon_{i\sigma}(\mathbf{k}) = \frac{1}{2} \left[ -x_{1\sigma} - x_{2\sigma} - (-1)^{i+1} \sqrt{(x_{1\sigma} - x_{2\sigma} - V)^2 + 4(\tilde{\Delta}_\sigma^2 + |\tilde{\gamma}_{0\mathbf{k}}|^2) - 4|\tilde{\gamma}_{0\mathbf{k}}| \sqrt{(x_{1\sigma} - x_{2\sigma} - V)^2 + 4\tilde{\Delta}_\sigma^2}} \right], \quad (35)$$

and

$$\epsilon_{j\sigma}(\mathbf{k}) = \frac{1}{2} \left[ -x_{1\sigma} - x_{2\sigma} - (-1)^{j+1} \sqrt{(x_{1\sigma} - x_{2\sigma} - V)^2 + 4(\tilde{\Delta}_\sigma^2 + |\tilde{\gamma}_{0\mathbf{k}}|^2) + 4|\tilde{\gamma}_{0\mathbf{k}}| \sqrt{(x_{1\sigma} - x_{2\sigma} - V)^2 + 4\tilde{\Delta}_\sigma^2}} \right], \quad (36)$$

where  $i = 1, 2$ ,  $j = 3, 4$ , and  $\tilde{\Delta}_\sigma = \Delta_\sigma + \gamma_1$ . Furthermore, we will show that the electronic band structure energies, given in Eqs. (35) and (36), are different for different spin orientations due to the presence of the external magnetic field  $B$

## B. Self-consistent equations and total energy

Indeed, for calculating numerically the electronic band structure and total energies related to the concrete spin direction, we need to solve a set of SC equations for the chemical potential ( $\mu$  in our theory is a physical quantity that we cal-

culate exactly after solving the SC equations), the average charge density difference function between the layers ( $\delta\bar{n} = \bar{n}_2 - \bar{n}_1$ ), and the excitonic order parameters  $\Delta_\uparrow$  and  $\Delta_\downarrow$  (those parameters are not equal  $\Delta_\uparrow \neq \Delta_\downarrow$ ). In Appendix A, we give the detailed derivation of the SC equations in the AA-BLG. Here, we just present the final form of those equations. We

get

$$\frac{1}{\kappa} = \frac{1}{N} \sum_{\mathbf{k}} \sum_{i=1}^4 \sum_{\sigma} (\alpha_{i\mathbf{k}\sigma} + \beta_{i\mathbf{k}\sigma}) n_F(\mu - \epsilon_{i\sigma}(\mathbf{k})),$$

$$\frac{\delta \bar{n}}{2} = \frac{1}{N} \sum_{\mathbf{k}} \sum_{i=1}^4 \sum_{\sigma} (\beta_{i\mathbf{k}\sigma} - \alpha_{i\mathbf{k}\sigma}) n_F(\mu - \epsilon_{i\sigma}(\mathbf{k})),$$

$$\Delta_{\sigma} = \frac{W(\Delta_{\sigma} + \gamma_1)}{N} \sum_{\mathbf{k}} \sum_{i=1}^4 \gamma_{i\mathbf{k}\sigma} n_F(\mu - \epsilon_{i\sigma}(\mathbf{k})). \quad (37)$$

The normalization factor  $N$  in Eqs. (37) is the number of the reciprocal lattice vectors  $\mathbf{k} = (k_x, k_y)$ . For each crystallographic direction  $k_i$  (with  $i = x, y$ ), we have chosen 100  $k_i$  points, thus totally having a number of  $N = 10^4$   $k_i$  points, considered in the numerical evaluations. The function  $n_F(x)$  entering the right-hand sides of the equations in Eqs. (37) is the Fermi-Dirac distribution function

$$n_F(x) = 1/(e^{\beta(x-\mu)} + 1), \quad (38)$$

where  $\mu$  is the chemical potential in the system and should be calculated exactly after solving the above SC equations. Particularly, the first equation in Eqs. (37) defines the chemical potential in the system (see, also, the discussion in Appendix A). The second of the equations in Eqs. (37) is the equation for density difference function  $\delta \bar{n}$ , which is defined in Eqs. (37) above. The  $\mathbf{k}$ -dependent parameters  $\alpha_{i\mathbf{k}\sigma}$ ,  $\beta_{i\mathbf{k}\sigma}$ , and  $\gamma_{i\mathbf{k}\sigma}$  are defined in Appendix A at the end of the paper. The third equation in Eqs. (37) is the subject of two separate SC equations for the excitonic order parameters  $\Delta_{\uparrow}$  and  $\Delta_{\downarrow}$ . The system of SC equations in Eqs. (37) could be solved with high precision by employing the finite-difference approximation method which retains the fast convergent Newton's algorithm [67].

The total  $\mathbf{k}$ -integrated sum of the single-excitation quasienergies in the region close to the first Brillouin zone is given by the expression

$$E_{\sigma} = \frac{1}{N} \sum_{\mathbf{k}} \sum_{i=1}^4 \epsilon_{i\sigma}(\mathbf{k}). \quad (39)$$

The results are plotted in Fig. 2 for both spin directions  $\sigma = \uparrow$  and  $\sigma = \downarrow$ . We have shown, in Fig. 2, the dependence of total energies  $E_{\sigma}$  on the magnetic field for different values of the normalized intralayer Coulomb interaction parameter  $U/\gamma_0$ . The plots in red show the total energies for two spin directions  $\sigma = \uparrow, \downarrow$  and for the small value of the Coulomb interaction parameter:  $U = \gamma_0 = 3$  eV. The plots in blue show the total energies for the large  $U$  limit with  $U = 4\gamma_0 = 12$  eV. We considered, in Fig. 2, the general case of the partial filling and put  $\kappa = 1$ . The interlayer Coulomb interaction parameter is set at the value  $W = 2\gamma_0 = 6$  eV and the external electric field potential is fixed at  $V = 2\gamma_0 = 6$  eV. We observe, in Fig. 2, that at zero value of the external magnetic field ( $\tilde{B} = 0$ ), the total energies are single valued for both values of the Coulomb interaction parameter  $U$ , i.e.,  $E_{\uparrow} = E_{\downarrow}$ . When augmenting the magnetic field  $\tilde{B} \neq 0$ , we get an effect similar to the usual spin-Zeeman one [29] and the energy bands, corresponding to different spin orientations, get split. Similar effects have been observed recently in Refs. [30,31], concerning the study

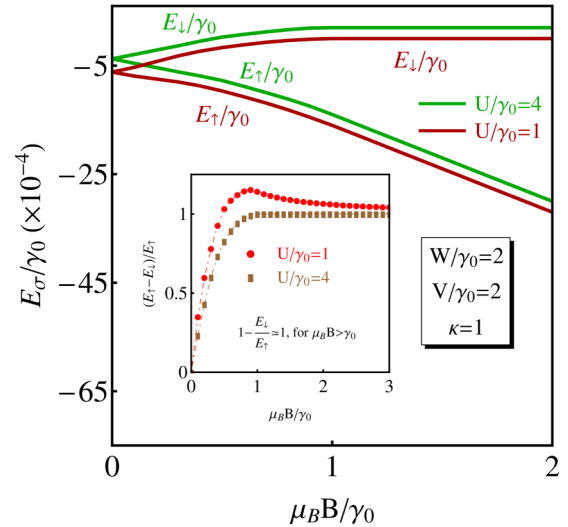


FIG. 2. Total  $\mathbf{k}$ -summed energies for different spin orientations  $E_{\uparrow}$  and  $E_{\downarrow}$  in AA-stacked bilayer graphene. We see in the picture the dependence on magnetic field  $B$ . Zeeman-like field splitting was observed for the nonzero values of the external magnetic field. Different limits of the intralayer Coulomb interaction parameter have been considered during the calculations. The lines in blue correspond to the case  $U = 4\gamma_0$  and the red lines correspond to the small value of the interaction parameter  $U = \gamma_0$ . The inverse filling coefficient  $\kappa$  was set at  $\kappa = 1$ , i.e., that is the case of partial filling. The temperature is set at  $T = 0$ .

of the magnetic field properties in AA-stacked BLG quantum dots and the energy spectrum of a magnetic quantum dot in graphene. The values of energy splitting depend on the strength of the external transverse magnetic field  $B$ . It is worth mentioning here that each point in Fig. 2 was calculated after solving the system of SC equations in Eqs. (37) (see next section) and putting the obtained values of the physical parameters  $\mu$ ,  $\delta \bar{n}$ ,  $\Delta_{\uparrow}$ , and  $\Delta_{\downarrow}$  in Eq. (38). For  $U = 3$  eV, the absolute value of the total splitting between  $E_{\uparrow}$  and  $E_{\downarrow}$  at  $\tilde{B} = 1$  is equal to  $\Delta E = |E_{\uparrow} - E_{\downarrow}| = 4.8$  meV. At the higher magnetic field  $\tilde{B} = 3$ , we get a large value for the splitting energy  $\Delta E = 14.4$  meV. We see in Fig. 2 that the variation of parameter  $U$  doesn't considerably change the total energy, corresponding to a given spin direction. In the inset in Fig. 2, we calculated the ratio  $\delta = (E_{\uparrow} - E_{\downarrow})/E_{\uparrow}$ . We observe that the ratio  $\delta$  increases continuously with  $\tilde{B}$  in the low magnetic field limit, i.e., when  $\tilde{B} \in (0, 1)$ . At high magnetic field values, i.e., when  $\tilde{B} \geq 1$ , the ratio  $\delta$  is stabilizing nearly to 1, i.e.,  $\delta \sim 1$  and the principal contribution to the total energy  $\Delta E$  is due to the spin direction  $\sigma = \downarrow$ .

## IV. NUMERICAL RESULTS

### A. Magnetic field effect

In the present section, we give the numerical results after solving the system of SC equations, given in Eqs. (37) at the end of the Sec. III. In Fig. 3, we solved the system of SC equations in Eqs. (37) for different values of the external magnetic field parameter  $\tilde{B} = \mu_B B/\gamma_0$ . In Fig. 3(a), we have shown the  $\tilde{B}$  dependence of the ratio of excitonic order

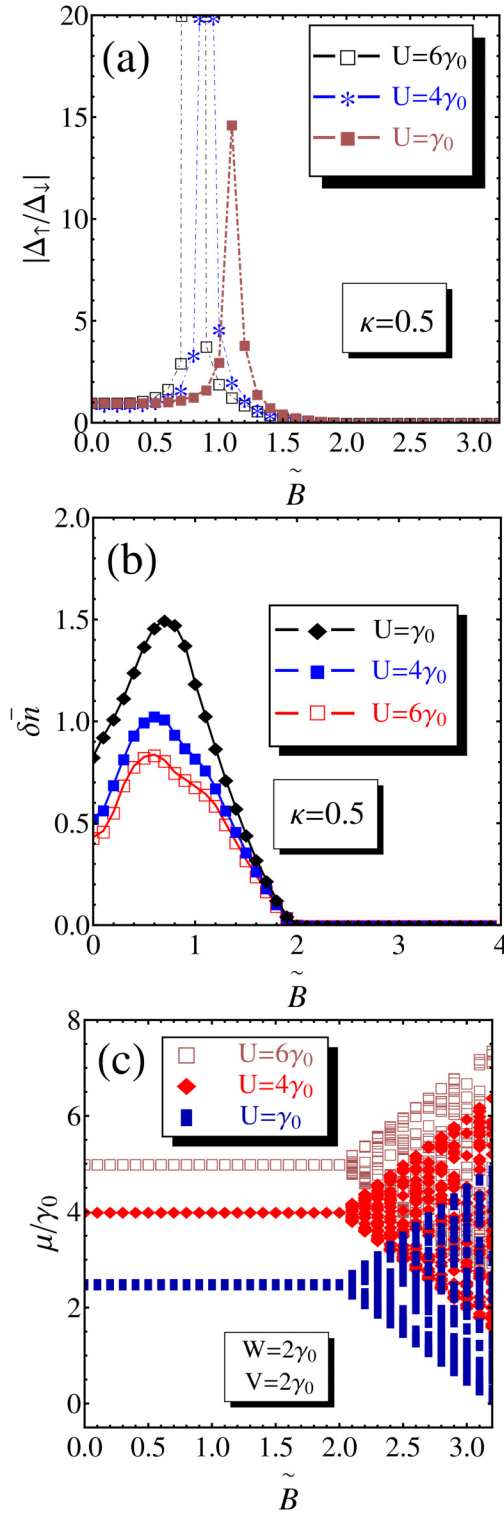


FIG. 3. The magnetic-field dependence of the principal physical parameters in the AA-BLG system. The results have been obtained after solving the set of self-consistent equations, given in Eqs. (37). In different panels, we have shown  $\tilde{B}$  dependence (with the magnetic field parameter  $\tilde{B} = \mu_B B/\gamma_0$ ) of (a) the ratio  $\delta = |\Delta_{\uparrow}/\Delta_{\downarrow}|$ , (b) the average charge density difference function between the layers  $\delta\bar{n}$ , and (c) the chemical potential. The interlayer Coulomb potential  $W$  is fixed at the value  $W = 2\gamma_0$ . The inverse filling coefficient is set at the value  $\kappa = 0.5$ , which corresponds to the half-filling regime, and the results have been plotted for  $T = 0$ .

parameters  $\Delta_{\uparrow}$  and  $\Delta_{\downarrow}$  defined as  $\delta = |\Delta_{\uparrow}/\Delta_{\downarrow}|$ . The inter-layer Hubbard potential is fixed at the value  $W = 2\gamma_0$ , the electric field potential is set at the value  $V = 2\gamma_0$ , and the half-filling case is considered here with  $\kappa = 0.5$ . It is clear from Fig. 3(a) that  $\Delta_{\uparrow} = \Delta_{\downarrow}$  for all limits of the intralayer Hubbard potential  $U$  considered in the picture. We observe in Fig. 3(a) that there exists a critical value of the magnetic field parameter  $\tilde{B}$ , above which the excitonic gap parameter  $\Delta_{\uparrow}$  vanishes, while  $\Delta_{\downarrow} \neq 0$  and the maximum difference between them is observed at the intermediate values of the external magnetic field  $\tilde{B} \in (1, 1.5)$ . Here we realize that the mentioned critical value is equal to  $\tilde{B}_C = 2$ . We see in Fig. 3(b) that the average charge density difference between the layers  $\delta_n$ , which defined the charge imbalance in the AA-BLG, vanishes at the same value  $\tilde{B}_C$  of the external magnetic field. We observe that for the small values of the external magnetic field, the parameter  $\delta_n$  is increasing, thus the average electron population in the top layer with  $\ell = 2$  (see Fig. 1 in Sec. II) increases with  $\tilde{B}$ , then it passes through a maximum (see the maximum of  $\delta\bar{n}$  at  $\tilde{B} = 0.9$  when  $U = \gamma_0$ ) and starts to decrease until the average CN occurs in the system:  $\delta\bar{n} = 0$ , which means that the average electron populations in both layers become equal, i.e.,  $\bar{n}_2 = \bar{n}_1$ , and the AA-BLG system becomes charge neutral. Thus the critical value  $\tilde{B}_C$  of the magnetic field could be called the CN point. The vanishing of parameter  $\delta\bar{n}$  could be important in many aspects of the applicability of the AA-BLG system as the nonperturbative structure device for use in modern nanomicroelectronics with the self-screened CN. Furthermore, in Fig. 3(c), we calculated the chemical potential  $\mu$  after SC equations in Eqs. (37). A very interesting degenerated behavior could be observed for the values of magnetic field parameter  $\tilde{B}$  in the interval  $\tilde{B} \in (0, \tilde{B}_C)$ . When  $\tilde{B} > \tilde{B}_C$ , this degeneracy is suppressed and a huge band solution appears at high magnetic field values. In Fig. 4, we presented the numerical results for the same parameters, as in Fig. 3, but for the case of partial filling with  $\kappa = 1$ . Moreover, we considered different limits of the interlayer Hubbard potential  $W$ . We observe in Figs. 3(a)–3(c) that the critical value of the magnetic field is smaller in this case with  $\tilde{B}_C = 1$ . Meanwhile, from the behavior of  $\delta\bar{n}$  in panel (b), in Fig. 3(b), it is clear that the CN never occurs in the limit of partial filling. Indeed, the parameter  $\delta\bar{n}$  never vanishes in this case [see Fig. 4(b)], but takes the constant values  $\delta\bar{n}_0$  when passing above the critical point  $\tilde{B}_C$ . Those constant values are different in different limits of the intralayer and interlayer Hubbard potentials and we observe a change in signs of  $\delta\bar{n}$  and  $\delta\bar{n}_0$  when passing from the high- $W$  limit to the small- $W$  limit (see, for example, the pair of plots in black and darker green). In the high- $(U, W)$  limit we have  $\delta\bar{n} > 0$  and  $\delta\bar{n}_0 > 0$ , while in the low- $(U, W)$  limit we get negative signs  $\delta\bar{n} < 0$  and  $\delta\bar{n}_0 < 0$ . The physical meaning of the observed behavior is simple: the fact that the average electron population in the top layer is higher (i.e.,  $\bar{n}_2 > \bar{n}_1$ ) or smaller ( $\bar{n}_2 < \bar{n}_1$ ) than the average electron population in the bottom layer depends on the strengths of the Hubbard interaction parameters  $U$  and  $W$ . Thus, by varying the interaction potentials, we can achieve the situation when the average electron population inversion takes place in the AA-BLG. Different constant values of the parameter  $\delta\bar{n}$  at  $\tilde{B} > \tilde{B}_C$  could also have their technological implementations as they imply

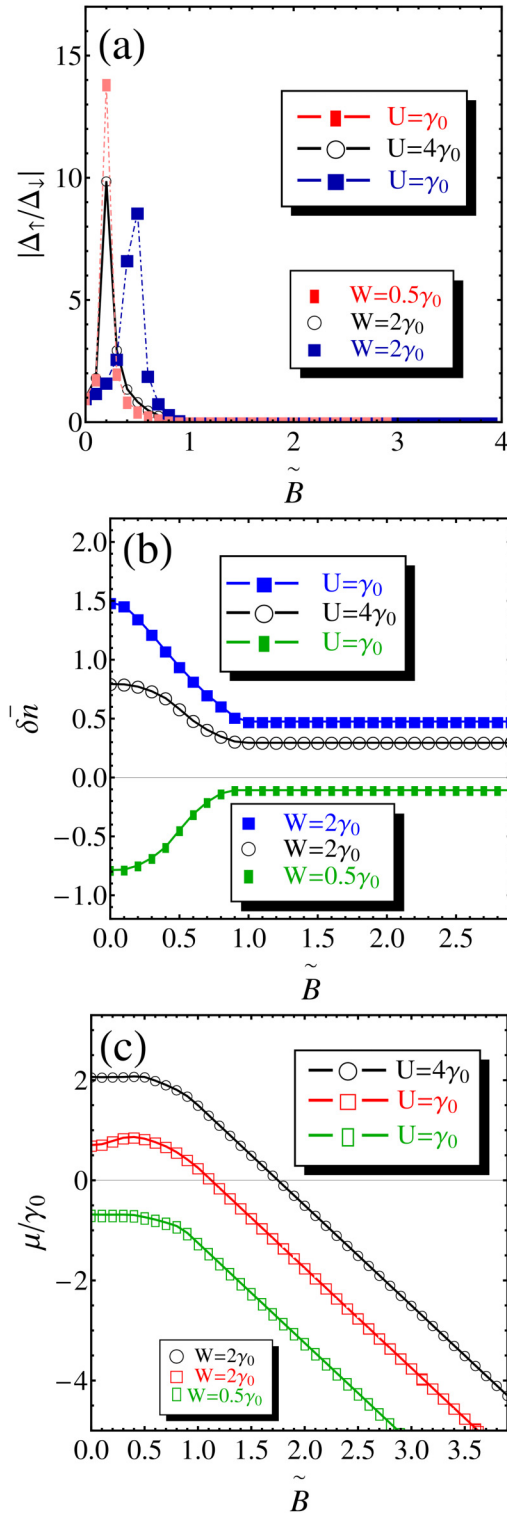


FIG. 4. The magnetic-field dependence of the principal physical parameters in the AA-BLG system. The results have been obtained after solving the set of self-consistent equations given in Eqs. (37). In different panels, we have shown  $\tilde{B}$  dependence (with the magnetic field parameter  $\tilde{B} = \mu_B B/\gamma_0$ ) of (a) the ratio  $\delta = |\Delta_{\uparrow}/\Delta_{\downarrow}|$ , (b) the average charge density difference function between the layers  $\delta\bar{n}$ , and (c) the chemical potential. Different limits of the Hubbard interaction potentials  $U$  and  $W$  have been considered. The inverse filling coefficient is set at the value  $\kappa = 1$ , which corresponds to the partial-filling regime, and the results have been plotted for  $T = 0$ .

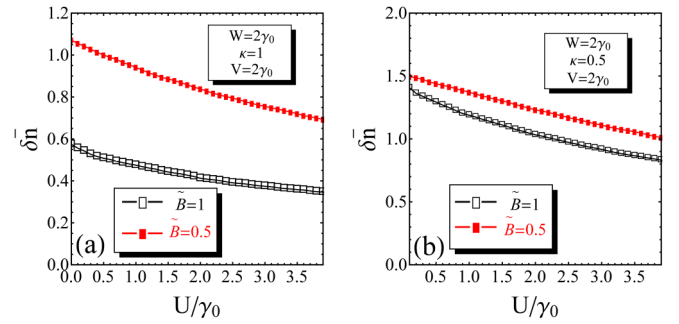


FIG. 5. The average charge density difference  $\delta\bar{n}$ , as a function of the intralayer Coulomb interaction parameter  $U$ . The results have been obtained after solving the set of self-consistent equations, given in Eqs. (37). In panels (a) and (b), we show the behavior of function  $\delta\bar{n}$  in the limit of partial filling with  $\kappa = 1$  and half-filling  $\kappa = 0.5$  (b). Different values of magnetic field parameter  $\tilde{B}$  have been considered in both panels. The interlayer Coulomb interaction potential  $W$  and electric field potential  $V$  are set at the values  $W = V = 2\gamma_0$ . The results have been obtained for  $T = 0$ .

that the AA-BLG system becomes a two-layer device with the desired average electron concentrations in different layers. In turn, the Hubbard interaction potentials could be tuned either by varying the applied electric field potential  $V$  or by changing the interlayer separation distance  $c_0$  in the AA-BLG.

Another important observation in Fig. 4 is related to the degenerated chemical potential  $\mu$  for all values of the applied magnetic field [see Fig. 4(c)]. Especially, the negative branch of the chemical potential solution at small values of the Hubbard interaction potentials [see the plot in darker green, in Fig. 4(c)] is a purposeful limit for the observation of the excitonic condensation phenomena in the AA-BLG system, i.e., when a macroscopic number of the excitonic pairs enter simultaneously into the fundamental states with the wave vector  $\mathbf{k} = 0$ . On the contrary, in the case of the half-filling regime considered in Fig. 3, such condensation is possible for magnetic fields up to the critical value  $\tilde{B}_C = 2$ . Moreover, we see in Fig. 4(c) that the chemical potential starts to decrease when passing through point  $\tilde{B}_C = 1$  and is always negative for small values of the Hubbard potentials  $U$  and  $W$ . Due to the fact that the excitonic order parameter  $\Delta_{\uparrow} = 0$ , for  $\tilde{B} > \tilde{B}_C$  we conclude that excitonic condensation in the AA-BLG system (with  $\mu < 0$ ) is due principally to the spin direction  $\sigma = \downarrow$  vis-à-vis the excitonic order parameter  $\Delta_{\downarrow}$ , remaining in this case [see Fig. 4(a)].

## B. Average charge density difference and interaction potentials

In Figs. 5 and 6, we show the local Hubbard interaction effects on the average charge density difference  $\delta\bar{n}$  for two different values of magnetic field parameter  $\tilde{B}$ . Particularly, in Fig. 5, we give the numerical results for  $\delta\bar{n}$  as a function of intralayer Hubbard potential  $U$ . The interlayer Hubbard potential is set at the value  $W = 2\gamma_0$  and the external gate potential is set at the value  $V = 2\gamma_0$ . The partial-filling and half-filling regimes have been considered in Fig. 5(a) with  $\kappa = 1$  and in Fig. 5(b) with  $\kappa = 0.5$ . In both cases, we observe a nearly linear decrease of  $\delta\bar{n}$  as a function of  $U$  and the average charge imbalance between

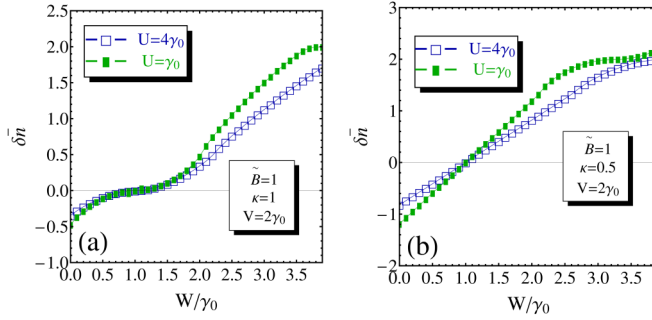


FIG. 6. The average charge density difference  $\delta\bar{n}$  as a function of the interlayer Coulomb interaction parameter  $W$ . The results have been obtained after solving the set of self-consistent equations given in Eqs. (37). In panels (a) and (b), we show the behavior of function  $\delta\bar{n}$  in the limit of partial filling with  $\kappa = 1$  (a) and half-filling  $\kappa = 0.5$  (b). Different values of interaction potential  $U$  have been considered in both panels. The electric field potential  $V$  is set at the value  $V = 2\gamma_0$ . The magnetic field parameter is fixed at the value  $\tilde{B} = 1$  and the results have been plotted for  $T = 0$ .

the layers is larger in the case of a small magnetic field (see the plots in red, corresponding to the magnetic field  $\tilde{B} = 0.5$ ). The general observation in Fig. 5 is that the intralayer Hubbard- $U$  potential is stabilizing the average charge imbalance between the layers, nevertheless, the CN never occurs in this case, even for the reasonably high values of parameter  $U$ .

Furthermore, in Fig. 6, we have calculated the average charge density difference  $\delta\bar{n}$  as a function of the interlayer Hubbard- $W$  interaction potential. Again, the partial-filling [see in Fig. 6(a)] and half-filling [see in Fig. 6(b)] regimes have been considered and the magnetic field is set at the value  $\tilde{B} = 1$ . The external gate potential is fixed at the value  $V = 2\gamma_0$ . We see that at the intermediate values of the interlayer Coulomb potential  $W_0$  (which depends on the parameter  $\kappa$ ), the function  $\delta\bar{n}$  crosses the  $W$  axis and  $\delta\bar{n} = 0$ . It is remarkable to note that the crossing point is the same for both strong and weak Hubbard- $U$  interaction limits and the function  $\delta\bar{n}$  changes its sign when passing through the CN point. Thus, by varying the interlayer Coulomb potential, we can tune the CN limit for function  $\delta\bar{n}$  and also achieve the average electron population reversion by the change of sign of the function  $\delta\bar{n}$ , i.e.,  $\delta\bar{n} < 0$  for  $W < W_0$  and  $\delta\bar{n} > 0$ , for  $W > W_0$ . It is also important to notice here that the function  $\delta\bar{n}$  is always increasing with  $W$ , which means that the high values of  $W$  bring the system out of the CN equilibrium position.

### C. The excitonic condensation and magnetic field

In Fig. 7, we have shown the  $\mathbf{k}$ -map for the excitonic order parameters  $\Delta_\uparrow(\mathbf{k})$  and  $\Delta_\downarrow(\mathbf{k})$  at the zero value of the external magnetic field, i.e.,  $\tilde{B} = 0$ . The half-filling case was considered during the numerical evaluations corresponding to the inverse filling parameter  $\kappa = 0.5$ . The other parameters are set as shown in the Fig. 7, i.e.,  $W = U = \gamma_0 = 3$  eV and  $\kappa = 0.5$  [see Fig. 7(a)],  $U = \gamma_0 = 3$  eV,  $W = 2\gamma_0$  and  $\kappa = 0.5$  [see Fig. 7(b)] and  $U = \gamma_0 = 3$  eV,  $W = 2\gamma_0$  and  $\kappa = 1$  [see Fig. 7(c)]. The external electric field potential is set at

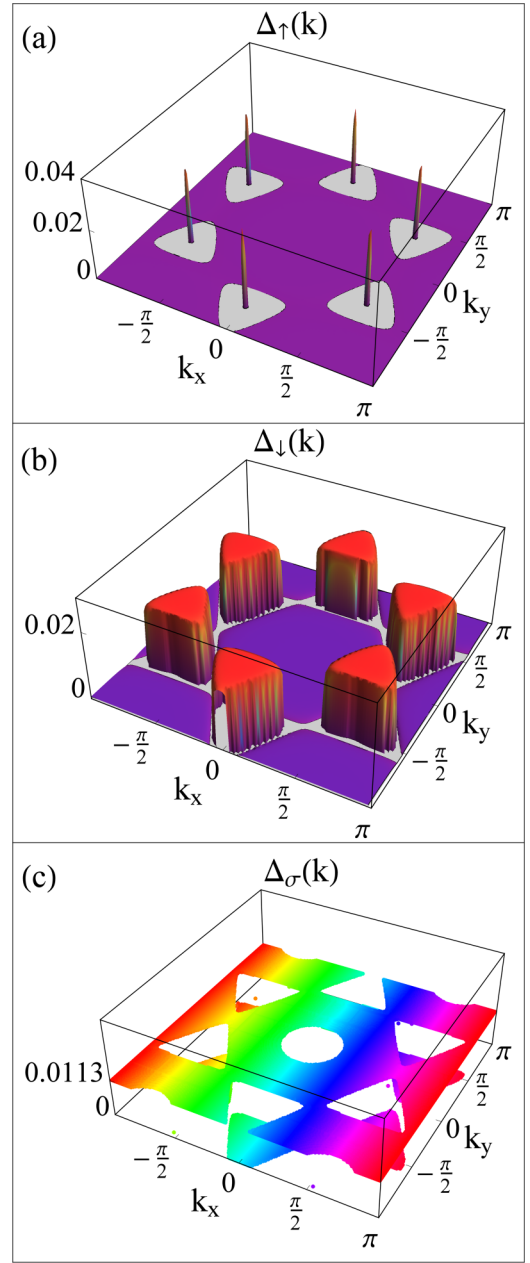


FIG. 7. The total  $\mathbf{k}$  map for the excitonic order parameter  $\Delta_\sigma(\mathbf{k})$ . The plots are shown for both spin directions  $\sigma = \uparrow, \downarrow$  and for the zero value of magnetic field  $\tilde{B} = 0$ . The other parameters are set as  $U = \gamma_0$ ,  $\kappa = 0.5$  and  $W = \gamma_0$  (a),  $U = \gamma_0$ ,  $\kappa = 0.5$  and  $W = 2\gamma_0$  (b), and  $U = \gamma_0$ ,  $\kappa = 1$  and  $W = 2\gamma_0$  (c). The large white sockets are formed in (a), which join each other in the form of hexagonal starlike hole-pocket (b) when increasing  $W$ . In the middle of the hole-star vertices (b), large exciton condensate peaks appear. The peaks coincide for different spin orientations. The plot for the case away from the half filling (this is the case of the partial-filling with  $\kappa = 1$ ) is shown in (c). The temperature is set at  $T = 0$ .

the value  $V = 2\gamma_0 = 6$  eV. We see that there are condensate peaks in the middle of the hexagonal sockets, formed in the reciprocal  $\mathbf{k}$  space for  $W = \gamma_0$ . When augmenting the interlayer interaction parameter [see Fig. 7(b)], the hexagonally arranged sockets are larger in this case and they stick together

by forming a starlike (with six vertices) pocket topology in the plane  $(k_x, k_y)$ . Moreover, in the middle of the starlike vertices, the large and dense exciton condensate peaks appear [see Fig. 7(b)]. We observe also that the excitonic order parameters corresponding to different spin orientations are equal, i.e.,  $\Delta_\uparrow = \Delta_\downarrow$ . Therefore, the interlayer Coulomb interaction influences considerably and contributes to the formation of the excitonic pairs and condensate states. In Fig. 7(c), we have evaluated the parameters  $\Delta_\uparrow$  and  $\Delta_\downarrow$ , away from the half-filling regime, and we put  $\kappa = 1$ . The interaction parameter  $W$  is set at the value  $W = 2\gamma_0$  as in the case of Fig. 7(b). We see in Fig. 7(c) that the holey starlike pocket topology is present in that case and, moreover, the excitonic pairing states are not zero in this limit and form a surface in the reciprocal space. The change in the order parameter  $\Delta_\sigma$  from the peaklike condensate structure to the surface of pairing could be attributed to the partial filling considered in Fig. 7(c) (with  $\kappa = 1$ ).

In Fig. 8, we give the  $\mathbf{k}$ -map for  $\tilde{B} = 1$  and for  $W = U = \gamma_0 = 3$  eV. We see that the magnetic field induces the differences between the excitonic order parameters  $\Delta_\uparrow$  and  $\Delta_\downarrow$  and  $\Delta_\uparrow \neq \Delta_\downarrow$ , in this case [see Figs. 8(a) and 8(b)]. Moreover, there exist excitonic pairings with low- and high-energy states in this case, which are shown in Figs. 8(a), 8(b) (with high energy excitonic states), and 8(c) (with low energy excitonic states). Particularly, in Fig. 8(a), the high energy excitonic states appear for  $\sigma = \uparrow$  in the form of separated red rings in the  $\mathbf{k}$  space. This topology of the excitonic pairing is furthermore transformed into the entire surfacelike pairing topology for  $\sigma = \downarrow$ . Moreover the excitonic condensate peaks appear on the light-blue background surface of excitonic pairing states with  $\sigma = \downarrow$  [see Fig. 8(b)]. These high-energy excitonic condensate peaks are more intense than the similar peaks in the case  $\tilde{B} = 0$  [see Fig. 8(b)]. In Fig. 8(c), we have shown the excitonic order parameters  $\Delta_\uparrow$  and  $\Delta_\downarrow$ , in the low-energy scale. We see that the topological disklike regions in pink [see Fig. 8(a) for  $\Delta_\uparrow$ ] and red [see Fig. 8(b) for  $\Delta_\downarrow$ ] appear in the form of two embedded cups (concavities) in Fig. 8(c). It follows from the picture in Fig. 8(c) that  $\Delta_\uparrow(\mathbf{k}) > \Delta_\downarrow(\mathbf{k})$  at the low-energy scale.

In Fig. 9, we have shown the  $\mathbf{k}$  map for the excitonic order parameters at the high magnetic field limit with  $\tilde{B} = 2$  at the half-filling case with  $\kappa = 0.5$ . In Fig. 9(a), the  $\mathbf{k}$  dependence is shown for the excitonic gap parameter  $\Delta_\uparrow(\mathbf{k})$ . The interlayer Coulomb interaction is set at the value  $W = 2\gamma_0$ . We see in Fig. 9 that a single, large excitonic condensate peak appears at the origin of the Brillouin zone, i.e., at the value of the reciprocal wave vector  $|\mathbf{k}| = 0$  [i.e., at the place of the condensate peak shown in Fig. 9(a)]. In Fig. 9(c), we have shown both order parameters ( $\Delta_\uparrow(\mathbf{k})$ ,  $\Delta_\downarrow(\mathbf{k})$ ) and we see how the excitonic condensate peak, observed in Fig. 9(a) merges with the excitonic pair formation surface [see Fig. 9(b)], exactly at the origin  $|\mathbf{k}| = 0$  of the reciprocal space.

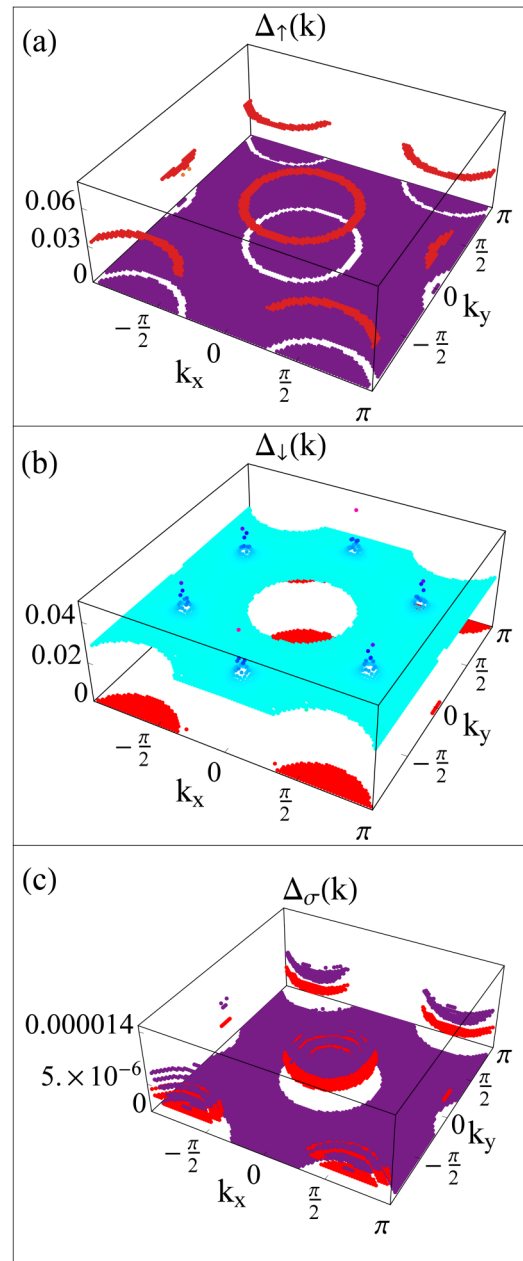


FIG. 8. The total  $\mathbf{k}$  map for the excitonic order parameter  $\Delta_\sigma(\mathbf{k})$ . The plots are shown for both spin directions  $\sigma = \uparrow, \downarrow$  and for the magnetic field  $\tilde{B} = 1$ . The other parameters are set as  $U = \gamma_0$ ,  $W = \gamma_0$ , and  $V = 2\gamma_0$ . Half-filling case is considered in the calculations, i.e.,  $\kappa = 0.5$  (one particle per site). The figures from left to right [(a)–(c)] show the  $\mathbf{k}$  map for  $\Delta_\uparrow(\mathbf{k})$  (a),  $\Delta_\downarrow(\mathbf{k})$  (b) and the mixture of them ( $\Delta_\uparrow(\mathbf{k})$ ,  $\Delta_\downarrow(\mathbf{k})$ ) [see in (c) the low-energy cutoff of previous images]. The excitonic order parameters are not the same for different spin orientations and exciton condensate peaks appear only in the case of  $\sigma = \downarrow$  [see the peaks on the light-blue background of the excitonic pair formation surface, in (b)]. The temperature is set at  $T = 0$ .

## D. Band structure

### 1. The role of the interlayer coupling

Hereafter, we present results for the electronic band structure in the AA-BLG system. The various values of the interlayer Coulomb interaction parameter  $W$  have been

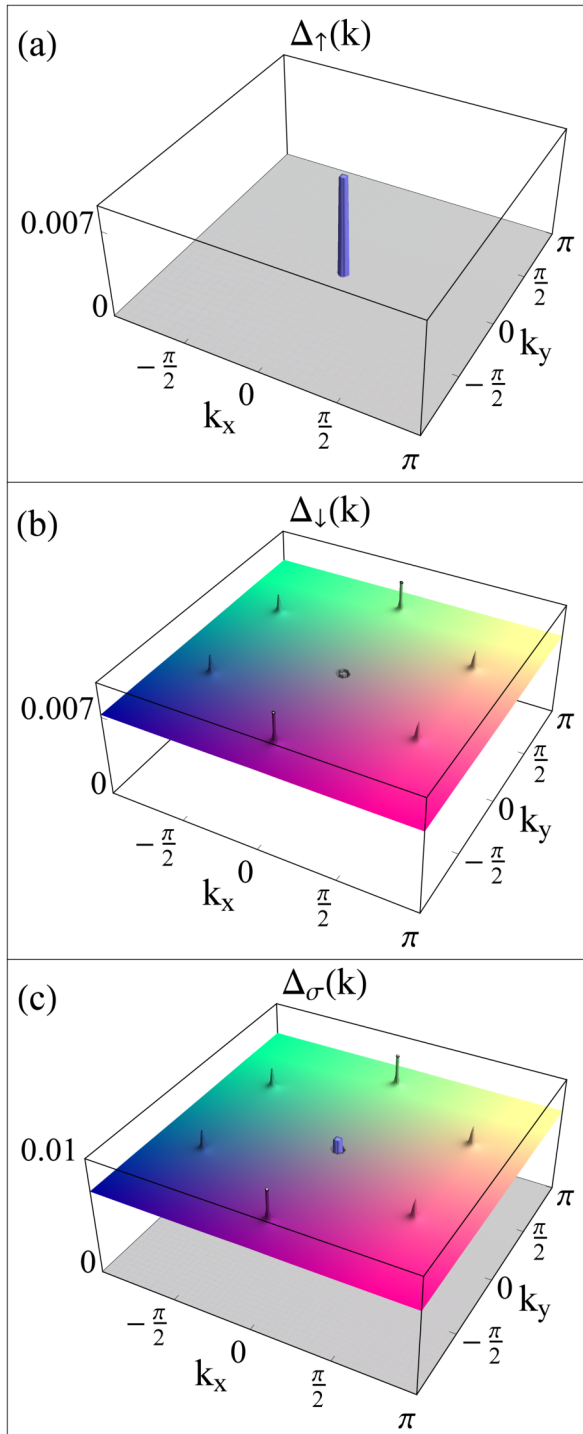


FIG. 9. The total  $\mathbf{k}$  map for the excitonic order parameter  $\Delta_\sigma(\mathbf{k})$ . The plots are shown for both spin directions  $\sigma = \uparrow, \downarrow$  and for the high magnetic field value  $\tilde{B} = 2$ . The other parameters are set as  $U = \gamma_0$ ,  $W = \gamma_0$ , and  $V = 2\gamma_0$ . Half-filling case is considered in the calculations, i.e.,  $\kappa = 0.5$  (one particle per-site). The figures from left to right [(a)–(c)] show the  $\mathbf{k}$  map for  $\Delta_\uparrow(\mathbf{k})$  (a),  $\Delta_\downarrow(\mathbf{k})$  (b), and the mixture of them [ $\Delta_\uparrow(\mathbf{k}), \Delta_\downarrow(\mathbf{k})$ ] (c). The excitonic gap parameters are not the same for different spin orientations and an isolated exciton condensate peak appears in (a) for  $\sigma = \uparrow$  at the origin of the  $\mathbf{k}$  space  $|\mathbf{k}| = 0$ . The excitonic pair formation regions are surrounded by the strongly pronounced condensate peaks for  $\sigma = \downarrow$  (b) and a hole remains at  $\mathbf{k} = 0$  for  $\Delta_\downarrow$ . The temperature is set at  $T = 0$ .

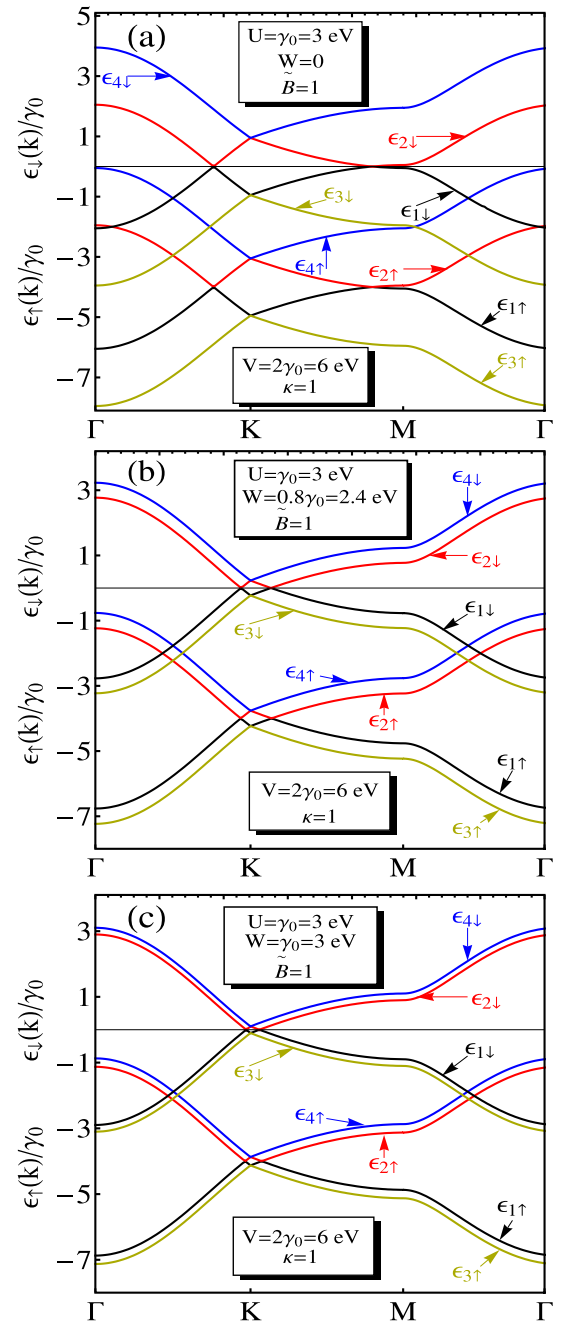


FIG. 10. The electronic band structure in AA bilayer graphene for different values of the interlayer Coulomb interaction parameter  $W$  [(a)–(c)]. The magnetic field is fixed at the value  $\tilde{B} = 1$  and the partial filling is considered in the layers with  $\kappa = 1$ . Eight different energy bands are shown in the pictures  $\epsilon_\uparrow(\mathbf{k}) \cup \epsilon_\downarrow(\mathbf{k})$  (see colored arrows near each energy band with the given spin direction). The temperature is set at  $T = 0$ .

considered in Fig. 10. For the other physical parameters in the system, we have chosen the following values:  $\tilde{B} = \mu_B B / \gamma_0 = 1$ ,  $U = \gamma_0 = 3$  eV, and  $\kappa = 1$  (the case of partial filling in the layers). The external electric gate potential is set at  $V = 2\gamma_0 = 6$  eV. The results plotted in Fig. 10 have been obtained for three different values of the interaction potential  $W$ :  $W = 0$  [see Fig. 10(a)],  $W = 0.8\gamma_0 = 2.4$  eV [Fig. 10(b)], and

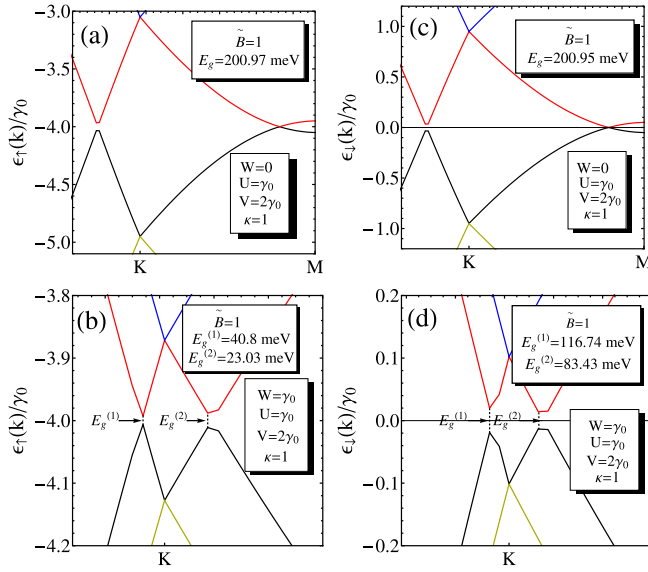


FIG. 11. The electronic band structure in AA bilayer graphene for different values of the interlayer Coulomb interaction parameter  $W$  [(a)–(f)]. The magnetic field is fixed at the value  $\tilde{B} = 1$  and the partial filling is considered in the layers with  $\kappa = 1$ . Four different energy bands are shown in different panels corresponding to each spin direction  $\sigma = \uparrow$  or  $\downarrow$ . The results of the band structure in left panels (a), (c), and (e) correspond to  $\sigma = \uparrow$  and the results in right panels (b), (d), and (f) correspond to  $\sigma = \downarrow$ . The narrow-range energy structure was shown in the panels, which demonstrates the band-gap opening in the electronic band structure. The band-gap opening is due to the effect of the interlayer Coulomb interaction  $W$ . The temperature is set at  $T = 0$ .

$W = U = \gamma_0 = 3$  eV Fig. 10(c)]. The band structure for both spin directions  $\sigma = \uparrow, \downarrow$  have been shown in the picture. To distinguish different energy branches (eight in our case) in Fig. 10, which correspond to different spin orientations  $\sigma = \uparrow, \downarrow$ , we have put small arrows near each energy band  $\epsilon_{i\sigma}(\mathbf{k})$  (with  $i = 1, \dots, 4$ ). We see that for the noninteracting layers, i.e., when  $W = 0$  [Fig. 10(a)], we have a big discrepancy between the band structures corresponding to different spin directions  $\sigma = \uparrow$  and  $\sigma = \downarrow$ . This effect of splitting is caused by the influence of the external magnetic field  $B$ . Furthermore, this displacement narrows for the nonzero values of the parameter  $W$  [see Figs. 10(b) and 10(c)]. Those band structures (for  $\sigma = \uparrow$  and  $\sigma = \downarrow$ ) get very close when  $W = U = \gamma_0 = 3$  eV [see Fig. 10(c)]. Thus, when  $U = W$  (this is the most realistic case when estimating the scales of Coulomb interactions in BLG structures), the region embedded between the linearly crossing energy bands gets very small. Additionally, we obtain a doubled number of such embedded regions [see in combined view  $\epsilon_{\uparrow}(\mathbf{k}) \cup \epsilon_{\downarrow}(\mathbf{k})$ ] due to the linear crossing (with no possible band gap) of the energy bands, corresponding to different spin directions. For all considered values of the interlayer Coulomb interaction parameter  $W$ , we have the intersections  $\epsilon_{2\uparrow} \cap \epsilon_{1\downarrow}, \epsilon_{2\uparrow} \cap \epsilon_{3\downarrow}, \epsilon_{4\uparrow} \cap \epsilon_{1\downarrow}, \epsilon_{4\uparrow} \cap \epsilon_{3\downarrow}$ . It is worth mentioning that those additional regions embedded in the middle of the intersection points are gapless for all values of parameter  $W$  and external magnetic field  $B$ . In Figs. 11(a)–11(d), the electronic band structure at the narrow regions of  $\epsilon_{\uparrow}(\mathbf{k})$  and  $\epsilon_{\downarrow}(\mathbf{k})$ , where the band gap is opening in the system. The

values of the physical parameters in the system are the same as in Fig. 10. We see in Figs. 11(a) and 11(c) that at  $W = 0$  a very large single band gap  $E_g$  opens in the system of order  $E_g = 200.97$  meV, for  $\sigma = \uparrow$  in the direction  $\Gamma \rightarrow K$  on the  $|\mathbf{k}|$  axis, and  $E_g = 200.95$  meV for  $\sigma = \downarrow$ .

The value of the band gap for  $\sigma = \uparrow$  decreases drastically for  $W = 0.8\gamma_0 = 2.4$  eV (with slightly displaced value of  $|\mathbf{k}|$  point in the direction  $\Gamma \rightarrow K$ ) and we have  $E_g^{(1)} = 67.38$  meV (see in panel (b), in Fig. 11(b)). Nevertheless, the value of the band gap is still very large for the spin direction  $\sigma = \downarrow$ , and we have  $E_g = 273.95$  meV. Moreover, for  $\sigma = \uparrow$ , a second smaller gap opens in the direction  $K \rightarrow M$  with the value  $E_g^{(2)} = 45.6$  meV. Indeed, this second gap in the direction  $K \rightarrow M$  is totally absent for the spin direction  $\sigma = \downarrow$  [Fig. 11(e)].

In Figs. 11(b) and 11(d), we considered the large value of the interlayer interaction parameter  $W$  and calculated the band structure for  $W = \gamma_0 = 3$  eV. The value of the band gap for  $\sigma = \uparrow$  decreases drastically for  $W = \gamma_0$ , attaining the value of order of  $E_g^{(1)} = 40.8$  meV [Fig. 11(b)], while in the channel  $\sigma = \downarrow$  the band gap still very large and we get  $E_g^{(1)} = 116.74$  meV [Fig. 11(d)]. Moreover, for both spin channels  $\sigma = \uparrow$  and  $\sigma = \downarrow$ , a second smaller gap  $E_g^{(2)}$  opens in the direction  $K \rightarrow M$  with the value  $E_g^{(2)} = 23.03$  meV for  $\sigma = \uparrow$  for the spin channel  $\sigma = \uparrow$  and we obtain a very large value for the second gap for  $\sigma = \downarrow$  with  $E_g^{(2)} = 83.43$  meV.

The band gap  $E_g^{(2)}$  for  $\sigma = \downarrow$  is greater from the value of  $E_g^{(1)}$  for  $\sigma = \uparrow$  by nearly a factor of 2. It is particularly worth mentioning that the distance  $|\Delta\mathbf{k}|$  between the  $|\mathbf{k}|$  points at which those two gaps are opening narrows for the large values of  $W$ , and this observation is true for both spin directions  $\sigma = \uparrow$  and  $\sigma = \downarrow$ . Due to the narrow energy range of excitations, those energy band gaps could be observed experimentally by fast light-emitting photon sources such as x-ray lasers [68]. Another important observation is related to the induced large excitation gap  $E_g^{(2)}$  (with the value of the gap  $E_g^{(2)} = 83.43$  meV) in the energy spectrum of  $\epsilon_{\downarrow}(\mathbf{k})$ , in the direction  $K \rightarrow M$  [see Fig. 11(d)] and nearly flat band-energy regions at the large value of  $W$ . Indeed, surprisingly, a sufficiently large  $\mathbf{k}$ -space region is found in the band structure corresponding to the direction of spin opposite to the magnetic field ( $\sigma = \downarrow$ ), where the usually crossing bands along direction  $K \rightarrow M$  get largely separated and flattened near the zero value of the energy axis [see Fig. 11(d)]. The general observation resulting from Fig. 11 is that the interlayer Coulomb interaction  $W$  plays a destructive role on the band gaps  $E_g^{(1)}$  for  $\sigma = \uparrow$  [Figs. 11(a) and 11(c)]. Thus, we have demonstrated in Fig. 11 that the increase of the interlayer interaction potential at the fixed nonzero value of the external magnetic field (experimentally, the changes in  $W$  could be realized by changing the separation distance between the layers [36] in the AA-BLG) has a destructive effect on the band gaps in the system and a phase transition from semiconducting to the weak-metallic state occurs in this case for the spin channel  $\sigma = \uparrow$ . This result is very similar with the results in Ref. [36].

## 2. The role of the magnetic field

In Fig. 12, we examined the role of the external magnetic field  $\tilde{B}$  on the electronic band structure and energy gaps in

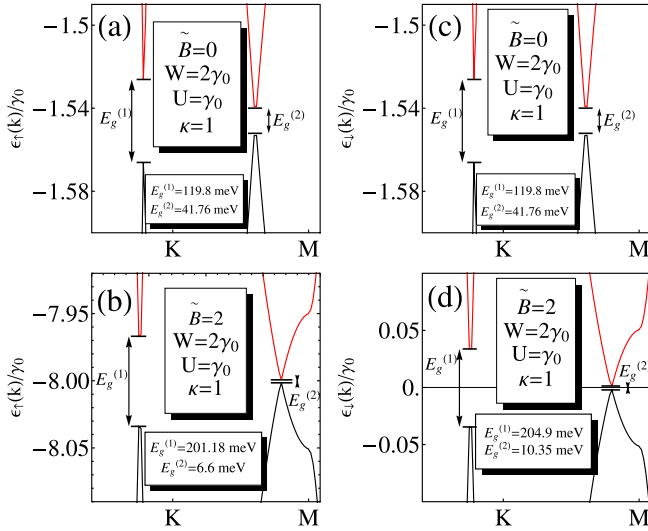


FIG. 12. The electronic band structure in AA bilayer graphene for different values of the external magnetic field  $\tilde{B}$  [see panels (a)–(f)]. The narrow-range energy structure is shown in panels, where we present the principal regions on the  $|\mathbf{k}|$  axis at which the band gap opens in the AA BLG. The band gaps in panels (a) and (d) at  $\tilde{B} = 0$  are due to the effect of the interlayer interaction parameter, which is fixed at the value  $W = 2\gamma_0 = 6$  eV. The partial-filling case is considered with  $\kappa = 1$ , and the temperature is set at  $T = 0$ .

the AA BLG and we considered both low [see Figs. 12(a) and 12(c)] and high magnetic field limits [see Figs. 12(b) and 12(d)]. We fixed the interaction parameter  $W$  to a sufficiently high value  $W = 2\gamma_0$ , and the partial-filling case is considered with the inverse filling coefficient  $\kappa = 1$ . The temperature is set at the value  $T = 0$  and the intralayer Coulomb interaction is set at the value  $U = \gamma_0$ . We see that even at  $\tilde{B} = 0$  there exist two gaps  $E_g^{(1)}$  and  $E_g^{(2)}$  in both energy spectrums  $\epsilon_{\uparrow}(\mathbf{k})$  and  $\epsilon_{\downarrow}(\mathbf{k})$  [see Figs. 12(a) and 12(c)] and they are exactly the same due to the spin-symmetry in the case and the absence of the Zeeman splitting. We obtain  $E_g^{(1)}(\sigma = \uparrow) = E_g^{(1)}(\sigma = \downarrow) = 119.8$  meV and  $E_g^{(2)}(\sigma = \uparrow) = E_g^{(2)}(\sigma = \downarrow) = 41.76$  meV. The second small gap  $E_g^{(2)}$  is comparable with the values of the band gap obtained via SOC interaction effects [17–20]. Next, when increasing the magnetic field parameter  $\tilde{B}$ , given in Figs. 12(b) and 12(d), the band gaps  $E_g^{(1)}$  for  $\sigma = \uparrow, \downarrow$  get increased considerably by approaching with their values to the band-gap energies in the usual direct band-gap semiconductors of type A<sup>III</sup>B<sup>IV</sup> or A<sup>IV</sup>B<sup>IV</sup> [48]; namely, we have  $E_g^{(1)}(\sigma = \uparrow) = 201.18$  meV,  $E_g^{(2)}(\sigma = \downarrow) = 204.9$  meV. The energy band gaps  $E_g^{(2)}$  decrease drastically for both spin channels and we obtain very small values of order of  $E_g^{(2)} = 6.6$  meV for  $\sigma = \uparrow$  and, for  $\sigma = \downarrow$ , we observe that  $E_g^{(2)} = 10.35$  meV. It is worth mentioning that the energy band gaps  $E_g^{(2)}$  obtained here are still much larger than the band gaps obtained in Refs. [17–20] when considering the SOC only. We observe in Fig. 12 that for the partial filling considered there (with  $\kappa = 1$ ), the semiconducting state is well-defined in the system for all values of the magnetic field parameter  $\tilde{B}$ .

Next we compare the results for the band gaps, obtained in Fig. 12, with the results of calculations at the half-filling

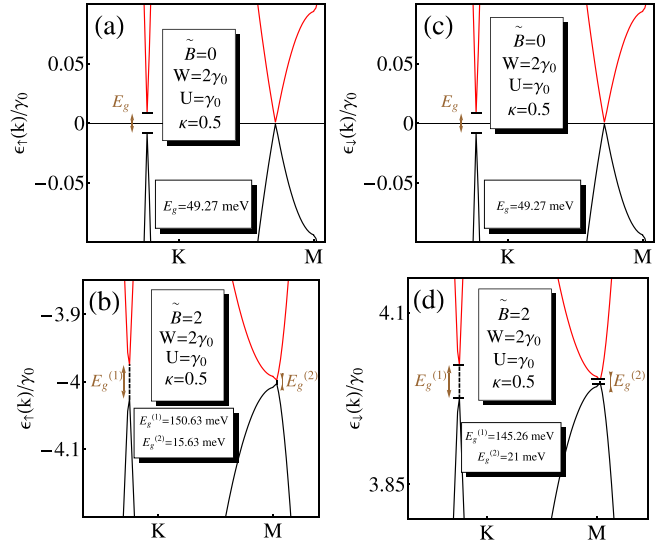


FIG. 13. Electronic band structure in AA bilayer graphene for different values of the interlayer Coulomb interaction parameter  $W$  [(a)–(f)]. The low-energy picture was shown here, corresponding to the band structure in Fig. 10. We show the principal regions, where the band gap is opening in the AA bilayer, caused by the effect of the interlayer Coulomb interaction. The magnetic field is fixed at the value  $\tilde{B} = \mu_B B / \gamma_0 = 1$ . Four different energy bands are shown in pictures for each spin direction. The results in top panels (a)–(c) correspond to  $\sigma = \uparrow$  and the results in the right panels (d)–(f) correspond to  $\sigma = \downarrow$ . The half-filling case is considered with  $\kappa = 0.5$ , and the temperature is set at  $T = 0$ .

limit, i.e., when  $\kappa = 0.5$  presented in Fig. 13. As we can see in Figs. 13(a)–13(c), the values of the gaps  $E_g^{(1)}$  are considerably smaller, in the case of zero magnetic field (we get  $E_g^{(1)} = 49.27$  meV for both spin channels), and the energy band gaps  $E_g^{(2)}$  are completely absent (i.e.,  $E_g^{(2)} = 0$ ) for  $\kappa = 0.5$  and  $\tilde{B} = 0$ .

The large values for  $E_g^{(1)}(\sigma)$  have been obtained in the limit of high magnetic fields with  $\tilde{B} = 2$  [see Figs. 13(b) and 13(d)] with  $E_g^{(1)}(\sigma = \uparrow) = 150.63$  meV and  $E_g^{(1)}(\sigma = \downarrow) = 145.26$  meV. Contrary to the previous case of partial filling ( $\kappa = 1$ ), we have a large decrease of the gaps  $E_g^{(1)}(\sigma = \uparrow)$  and  $E_g^{(2)}(\sigma = \downarrow)$  for all values of the external magnetic field  $\tilde{B}$ . Thus, for the half-filling case (with  $\kappa = 0.5$ ), the increase of the magnetic field parameter leads to the passage from the weak-metallic state into the semiconducting one.

### E. Discussion and perspectives

The results obtained for the excitonic order parameters for different spin directions above show that the AA-BLG system could be an ideal candidate for the observation of the excitonic condensation phenomena at  $T = 0$ . Particularly, in Fig. 9, the excitonic condensate peak was observed in the centrum of the  $\mathbf{k}$  space and for the large value of the magnetic field parameter. The numerical results presented in Figs. 10–13 show the large applicabilities of the biased AA-BLG systems when it is exposed to the action of the external transverse magnetic field  $B$  (see Fig. 1). Based on the appropriate parameter regime,

discussed in the previous sections, AA-BLG could be a purposeful candidate for applications in modern nanotechnology and solid-state electronics as a direct band-gap semiconductor with a fully tunable band structure and band gaps. Both the Coulomb interaction (which could be tuned by varying the interlayer separation distance [29]) and the magnetic field tunability could be used to obtain the large energy gaps in the energy spectrum of the AA-BLG. Choosing the parameters to be tuned in the system (for example,  $W$  or magnetic field  $\tilde{B}$ ), we can open or close the band gaps corresponding to  $\sigma = \uparrow$  or  $\sigma = \downarrow$ , which can result in excitation states with only one spin direction  $\sigma = \uparrow$  or  $\sigma = \downarrow$ . This type of situation is achieved in Figs. 11(a)–11(d) when, by increasing the interaction parameter  $W$  and fixing the magnetic field (namely, at the value  $\tilde{B} = 1$ ), we close the energy band gap for the spin direction  $\sigma = \uparrow$  [Figs. 11(a) and 11(b)], while the other energy gap corresponding to  $\sigma = \downarrow$  is still very large for all values of parameter  $W$  [see Figs. 11(c) and 11(d), in the picture], comparable to those in direct band-gap semiconductors [48]. Thus, for the spin direction  $\sigma = \uparrow$  we get, in Fig. 11, an inverse transition from semiconducting state into the metallic one [Figs. 11(a)–11(c)]. Moreover, in Figs. 12 and 13, we found transitions of weak metal-semiconductor and metal-semiconductor types when tuning the magnetic field parameter up to high values. In practice, this type of spin-selective operation mode, with the appropriate band-gap excitations, could be achieved by regulating the photon's emitters (with the appropriate range of wavelength selection) at the corresponding modes ( $|\mathbf{k}|_{\text{ph}}, \Omega_{\text{ph}}$ ), where the components  $|\mathbf{k}|_{\text{ph}}$  and  $\Omega_{\text{ph}}$  determine the crystallographic direction and the corresponding frequency (or energy) of photons emitted by the source. Thus, the AA-BLG could also be applied as a spin-valve device, where, in one spin direction, we get the blockage of the electron transport [see the results in Figs. 11(c) and 11(d) for  $\sigma = \downarrow$ ], while in another spin channel  $\sigma = \uparrow$  we get the possibilities for the electron excitations into the conduction band and electronic transport [see Fig. 11(b) for  $\sigma = \uparrow$ ]. Such a spin-controlled transport in AA-BLG demonstrated here and the spin-valve effects could also be purposeful for building the new quantum algorithms, important for quantum computations and quantum information theory.

The results presented here have been performed at the zero-temperature limit. We have shown the AA-BLG system is purposeful for obtaining the stable excitonic condensate states and the metal-semiconductor or semiconductor-metal transitions at zero temperature limit. In this context, the room temperature excitonic and metal-semiconducting transitions in AA-BLG will represent fundamental steps toward new possibilities for fast and safe electronics and quantum information.

## V. CONCLUDING REMARKS

In the present paper, we considered the effects of external magnetic and electric fields on the physical properties in AA-stacked excitonic BLG. By using the bilayer generalization of the usual Hubbard model, we derived a set of SC equations for the excitonic order parameters, the average charge density difference between the layers and the chemical potential in

the system. Both partial and half-filling regimes have been discussed and the role of the Hubbard interactions has been revealed. We have calculated the magnetic field dependence of those quantities and found the critical value of the magnetic field at which the CN occurs in the system at the half-filling regime. Moreover, we have shown that above that critical value, the excitonic order parameter for the spin direction  $\sigma = \uparrow$  gets quenched, which opens the possibility for the spin-controlled electronic transport in the AA-BLG structure and its use as a spin-valve device in modern nanotechnology. Furthermore, the behavior of the chemical potential in the partial-filling regime shows explicitly the possibilities for the excitonic condensation of the preformed excitonic pairs in such a system. Additionally, the role of the Hubbard interaction potentials on the average charge density imbalance function has been analyzed and the principal differences between the actions of the Hubbard- $U$  and Hubbard- $W$  couplings have been discussed.

Indeed, we studied the out-of-plane magnetic field, which causes the Zeeman splitting. Moreover, we considered the case of the uniform and static magnetic field. For this reason, we neglected the orbital magnetic field, which is generally included in the form of the Peierls phases, associated to the electrons.

We have shown the effects of the external transverse magnetic field on the excitonic pair formation and condensation in the AA-stacked BLG structure. An ideally isolated excitonic condensate peak appears for the large values of the magnetic field and the excitonic pairing regions have been found in the reciprocal space, corresponding to both spin directions. We have found that the excitonic order parameters with the spin directions opposite to the magnetic field are in general larger than those corresponding to the spin direction parallel to the magnetic field. We have calculated the electronic band structure for different values of the external magnetic field  $B$  and interlayer Coulomb interaction parameter  $W$ . We showed that both contribute considerably to the energy spectrum in AA-BLG and result in the opening of the large energy band gaps in the system comparable to the known values of the band gaps in the usual semiconducting heterojunctions [48]. We observed that the energy band gaps are large for the spin direction opposite to the external magnetic field and this observation is true for most values of the magnetic field and interlayer Coulomb interaction parameter considered in the paper. We have demonstrated that a very-large band gap is opening (with  $E_g = 200.97$  meV) even for the noninteracting layers (i.e., when  $W = 0$ ) when the external magnetic field is present,  $B \neq 0$ . Furthermore, when augmenting the interlayer interaction potential at the same fixed value of the external magnetic field, the band gap decreases for  $\sigma \uparrow \uparrow \mathbf{B}$  (up to the value  $E_g^{(\uparrow)} = 40.8$  meV) and is still very large for the spin directions opposite to the magnetic field  $\sigma \downarrow \uparrow \mathbf{B}$  (with  $E_g^{(\downarrow)} = 116.74$  meV). We have shown that even at  $B = 0$  a very large energy band gap opens in the energy spectrum when considering the interlayer Coulomb interaction  $W \neq 0$ . Particularly, when  $W = 2\gamma_0 = 6$  eV, we get  $E_g^{(\uparrow)} = E_g^{(\downarrow)} = 119.8$  meV, for partial-filling  $\kappa = 1$  and  $E_g^{(\uparrow)} = E_g^{(\downarrow)} = 49.27$  meV, for the half-filling regime with  $\kappa = 0.5$ . Furthermore, these gaps become large when augmenting the magnetic field parameter. For  $\tilde{B} = 2$ , we get very

large values for the band-gap parameter  $E_g$ , for both limits of the average electron occupation numbers at the atomic lattice sites positions (partial filling and half filling). For the partial filling, we get  $E_g^{(\uparrow)} = 201.18$  meV and  $E_g^{(\downarrow)} = 204.9$  meV. For the half-filling regime, we get  $E_g^{(\uparrow)} = 150.63$  meV and  $E_g^{(\downarrow)} = 145.26$  meV. The general observation coming from our calculations is that the energy band gap is smaller for the half-filling case and  $E_g^\sigma(\kappa = 0.5) < E_g^\sigma(\kappa = 1)$ . Moreover, a second energy band gap opens near the value of the reciprocal wave vector  $|\mathbf{k}| = M(2\pi/3, 0)$  (point  $M$ , at which the usual linear bands cross in the ungapped pristine AA-BLG) and we have also discussed the values of this second energy-gap in the paper. The second small band gap is zero only in the regimes when  $\tilde{B} \neq 0, W = 0$  (for the partial filling) or  $B = 0, W \neq 0$  (for the half filling). Thus, we have shown the possibility of a metal-semiconductor transition in the biased AA-BLG in the presence of the external transverse magnetic field  $B$ . We have shown that such transition could happen either by changing the interlayer interaction potential (at partial filling and with fixed value of the magnetic field) or by changing the applied magnetic field with the fixed value of the interlayer potential (in the case of half filling). Additionally, we established that the semiconducting state is much stronger in the limit of partial filling, i.e., when  $\kappa = 1$ .

The calculations presented here are still valid for a very large interval of temperatures, although the results are not shown here. Therefore, the results obtained within this paper could also be useful for studies of the excitonic condensate states and could help also the experimenters to find the excitonic condensates regimes, not yet observed experimentally in graphene-based heterostructures. The results obtained in the present paper concern the artificially obtained AA-BLG heterostructures (obtained by deposition from single graphene layers) rather than the pristine or epitaxially obtained BLG.

The spin-selective band-gap formation in the AA-BLG structure, observed in the present paper, opens a very interesting future for technological applications of AA-BLG as systems with spin-valve effect, as quantum spin selectors for quantum nanoelectronics, as spin-controlled electronic transistors, quantum spin-transport systems for quantum information applications, and as the spin-injector systems. In our strong conviction, the AA-BLG system under the external field conditions discussed in the present paper could compete with Bernal stacked AB-BLG structures due to the large values of the energy band gaps, approaching the band-gap parameters in the usual direct band-gap semiconducting materials [48]. Another interesting observation resulting from our calculations is that the AA-BLG system considered here could be used as a system in which the perfect excitonic condensate states could be observed experimentally in the high magnetic field limit.

#### APPENDIX A: SELF-CONSISTENT EQUATIONS FOR AA-BLG

In the present Appendix, we give the details of calculations of the set of SC equations in the considered AA-BLG system, discussed in Sec. III B. In the real-space notations, those SC

equations read as

$$\begin{aligned} \bar{n}_a + \bar{n}_{\bar{a}} &= \frac{1}{\kappa}, \\ \bar{n}_{\bar{a}} - \bar{n}_a &= \frac{\delta\bar{n}}{2}, \\ \Delta_\sigma &= W \langle \bar{a}_\sigma(\mathbf{r}\tau) a_\sigma(\mathbf{r}\tau) \rangle. \end{aligned} \quad (\text{A1})$$

The average fermionic densities  $\bar{n}_a$ , and  $\bar{n}_{\bar{a}}$  are given as  $\bar{n}_a = \bar{n}_{a\uparrow} + \bar{n}_{a\downarrow}$  and  $\bar{n}_{\bar{a}} = \bar{n}_{\bar{a}\uparrow} + \bar{n}_{\bar{a}\downarrow}$ . Here, we have considered the excitonic order parameter  $\Delta_\sigma$  as real, i.e.,  $\Delta_\sigma = \bar{\Delta}_\sigma$ . This corresponds to the case of a homogeneous AA-BLG system, where the pairing between electrons and holes is translationally invariant. The first equation in the system of equations in Eqs. (A1) defines the dynamical chemical potential, which should be calculated numerically. The second equation in the system in Eqs. (A1), is written for the average charge density difference  $\delta\bar{n}$  (with  $\delta\bar{n} = \bar{n}_2 - \bar{n}_1$ ) between the layers in the AA-BLG.

For calculating the fermionic Green's functions, we rewrite the expression of the partition function in terms of the Grassmann-Nambu spinors introduced in Sec. III A,

$$\mathcal{Z} = \int [D\bar{\Psi}][D\Psi] e^{-S[\bar{\Psi}, \Psi]}, \quad (\text{A2})$$

where the action in exponential on the right-hand side in Eq. (A2) is given in Eq. (17) in Sec. II A. Taking into account two spin directions  $\sigma = \uparrow, \downarrow$ , we can rewrite for  $\mathcal{Z}$  the following expression:

$$\mathcal{Z} = \mathcal{Z}_\uparrow \mathcal{Z}_\downarrow. \quad (\text{A3})$$

Furthermore, for the considered spin  $\sigma$ , we write each component in the product in Eq. (A3) in their general forms, which include the auxiliary sources  $J(\mathbf{k}v_n)$  and  $\bar{J}(\mathbf{k}v_n)$ :

$$\begin{aligned} \mathcal{Z}_\sigma &= \int [D\bar{\Psi}_\sigma][D\Psi_\sigma] e^{-\frac{1}{2} \sum_{\mathbf{k}v_n} \bar{\Psi}_\sigma(\mathbf{k}v_n) \mathcal{G}_\sigma^{-1}(\mathbf{k}v_n) \Psi_\sigma(\mathbf{k}v_n)} \\ &\times e^{\frac{1}{2} \sum_{\mathbf{k}v_n} \bar{\Psi}_\sigma(\mathbf{k}v_n) J_\sigma(\mathbf{k}v_n) + \Psi_\sigma(\mathbf{k}v_n) \bar{J}_\sigma(\mathbf{k}v_n)}. \end{aligned} \quad (\text{A4})$$

The auxiliary sources  $J_\sigma(\mathbf{k}v_n)$  and  $\bar{J}_\sigma(\mathbf{k}v_n)$  are the Grassmann-Nambu spinors with four components, which are defined in the same way as the spinors  $\bar{\Psi}(\mathbf{k}v_n)$  and  $\Psi(\mathbf{k}v_n)$ . Then, we effectuate the HS transformation for the four-component Grassmann fields  $\bar{\Psi}$  and  $\Psi$ , in the same way as it is done usually for two-component fermionic field [69]. We get for the two components  $\mathcal{Z}_\uparrow$  and  $\mathcal{Z}_\downarrow$  in Eq. (A3)

$$\begin{aligned} \mathcal{Z}_\uparrow &= \frac{1}{\prod_{\mathbf{k}v_n} \det \mathcal{G}_\uparrow(\mathbf{k}v_n)} e^{\frac{1}{2} \sum_{\mathbf{k}v_n} \bar{J}_\uparrow(\mathbf{k}v_n) \mathcal{G}_\uparrow(\mathbf{k}v_n) J_\uparrow(\mathbf{k}v_n)}, \\ \mathcal{Z}_\downarrow &= \frac{1}{\prod_{\mathbf{k}v_n} \det \mathcal{G}_\downarrow(\mathbf{k}v_n)} e^{\frac{1}{2} \sum_{\mathbf{k}v_n} \bar{J}_\downarrow(\mathbf{k}v_n) \mathcal{G}_\downarrow(\mathbf{k}v_n) J_\downarrow(\mathbf{k}v_n)}. \end{aligned} \quad (\text{A5})$$

The functions  $\mathcal{G}_\sigma(\mathbf{k}v_n)$  in Eqs. (A5) are the Green's functions for our problem. Furthermore, the set of SC equations in

Eqs. (A1) will be rewritten in the following expanded form:

$$\begin{aligned}\frac{1}{\kappa} &= \frac{1}{\beta N} \sum_{\mathbf{k}v_n} \sum_{m=1,3} \sum_{\sigma} \frac{A_{mm\sigma}(\mathbf{k}v_n)}{\det \mathcal{G}_{\sigma}^{-1}(\mathbf{k}v_n)}, \\ \frac{\delta \bar{n}}{2} &= \frac{1}{\beta N} \sum_{\mathbf{k}v_n} \sum_{m=1,3} \sum_{\sigma} i^{m+1} \frac{A_{mm\sigma}(\mathbf{k}v_n)}{\det \mathcal{G}_{\sigma}^{-1}(\mathbf{k}v_n)}, \\ \Delta_{\sigma} &= \frac{W}{\beta N} \sum_{\mathbf{k}v_n} \frac{A_{13\sigma}(\mathbf{k}v_n)}{\det \mathcal{G}_{\sigma}^{-1}(\mathbf{k}v_n)}.\end{aligned}\quad (\text{A6})$$

The functions  $A_{11\sigma}(x)$ ,  $A_{33\sigma}(x)$ , and  $A_{13\sigma}(x)$  in the numerators, on the right-hand sides of these equations, are indeed

the polynomials of third [ $A_{11\sigma}(x)$  and  $A_{33\sigma}(x)$ ] and second [ $A_{13\sigma}(x)$ ] orders. They are given as

$$\begin{aligned}A_{11\sigma}(x) &= x^3 + a_{1\sigma}x^2 + b_{1\sigma}(\mathbf{k})x + c_{1\sigma}(\mathbf{k}), \\ A_{33\sigma}(x) &= x^3 + a_{2\sigma}x^2 + b_{2\sigma}(\mathbf{k})x + c_{2\sigma}(\mathbf{k}), \\ A_{13\sigma}(x) &= a_{3\sigma}x^2 + b_{3\sigma}x + c_{3\sigma}(\mathbf{k}),\end{aligned}\quad (\text{A7})$$

where  $x = -iv_n$  and the coefficients  $a_{i\sigma}, b_{i\sigma}, c_{i\sigma}$  with  $i = 1, 2, 3$  are expressed with the help of parameters  $x_{i\sigma}$  defined in Eqs. (28) in Sec. III A. We obtained

$$\begin{aligned}a_{1\sigma} &= x_{1\sigma} + 2x_{2\sigma} + \frac{V}{2}, \\ b_{1\sigma}(\mathbf{k}) &= 2x_{1\sigma}x_{2\sigma} + x_{2\sigma}^2 + x_{1\sigma}V - \frac{V^2}{4} - \tilde{\Delta}_{\sigma}^2 - |\tilde{\gamma}_{\mathbf{k}}|^2, \\ c_{1\sigma}(\mathbf{k}) &= \frac{1}{8}[-(V + 2x_{2\sigma})(V^2 + 2x_{2\sigma}V - 2x_{1\sigma}(2x_{2\sigma} + V) + 4\tilde{\Delta}_{\sigma}^2) + 4(V - 2x_{1\sigma})|\tilde{\gamma}_{\mathbf{k}}|^2], \\ a_{2\sigma} &= x_{2\sigma} + 2x_{1\sigma} - \frac{V}{2}, \\ b_{2\sigma}(\mathbf{k}) &= 2x_{1\sigma}x_{2\sigma} + x_{1\sigma}^2 - x_{2\sigma}V - \frac{V^2}{4} - \tilde{\Delta}_{\sigma}^2 - |\tilde{\gamma}_{\mathbf{k}}|^2, \\ c_{2\sigma}(\mathbf{k}) &= \frac{1}{8}[(-V + 2x_{1\sigma})(-V^2 - 2x_{2\sigma}V + 2x_{1\sigma}(2x_{2\sigma} + V) - 4\tilde{\Delta}_{\sigma}^2) - 4(V + 2x_{2\sigma})|\tilde{\gamma}_{\mathbf{k}}|^2], \\ a_{3\sigma} &= \tilde{\Delta}_{\sigma}, \\ b_{3\sigma} &= (x_{1\sigma} + x_{2\sigma})\tilde{\Delta}_{\sigma}, \\ c_{3\sigma}(\mathbf{k}) &= \frac{\tilde{\Delta}_{\sigma}}{4}[(2x_{1\sigma} - V)(2x_{2\sigma} + V) + 4|\tilde{\gamma}_{\mathbf{k}}|^2].\end{aligned}\quad (\text{A8})$$

Next, after summing over the fermionic Matsubara frequencies  $v_n$  in Eqs. (A6), we get the system of SC equations, in Eqs. (37), in Sec. III B. The coefficients  $\alpha_{i\mathbf{k}\sigma}$ ,  $\beta_{i\mathbf{k}\sigma}$ , and  $\gamma_{i\mathbf{k}\sigma}$  (with  $i = 1, \dots, 4$ ) in Eqs. (37) are defined with the help of the polynomials in Eqs. (A7). We obtain

$$\alpha_{i\mathbf{k}\sigma} = (-1)^{i+1} \begin{cases} \frac{A_{11\sigma}(\epsilon_{i\sigma}(\mathbf{k}))}{\epsilon_{1\sigma}(\mathbf{k}) - \epsilon_{2\sigma}(\mathbf{k})} \prod_{j=3,4} \frac{1}{\epsilon_{i\sigma}(\mathbf{k}) - \epsilon_{j\sigma}(\mathbf{k})}, & \text{if } i = 1, 2 \\ \frac{A_{11\sigma}(\epsilon_{i\sigma}(\mathbf{k}))}{\epsilon_{3\sigma}(\mathbf{k}) - \epsilon_{4\sigma}(\mathbf{k})} \prod_{j=1,2} \frac{1}{\epsilon_{i\sigma}(\mathbf{k}) - \epsilon_{j\sigma}(\mathbf{k})}, & \text{if } i = 3, 4, \end{cases}\quad (\text{A9})$$

$$\beta_{i\mathbf{k}\sigma} = (-1)^{i+1} \begin{cases} \frac{A_{33\sigma}(\epsilon_{i\sigma}(\mathbf{k}))}{\epsilon_{1\sigma}(\mathbf{k}) - \epsilon_{2\sigma}(\mathbf{k})} \prod_{j=3,4} \frac{1}{\epsilon_{i\sigma}(\mathbf{k}) - \epsilon_{j\sigma}(\mathbf{k})}, & \text{if } i = 1, 2 \\ \frac{A_{33\sigma}(\epsilon_{i\sigma}(\mathbf{k}))}{\epsilon_{3\sigma}(\mathbf{k}) - \epsilon_{4\sigma}(\mathbf{k})} \prod_{j=1,2} \frac{1}{\epsilon_{i\sigma}(\mathbf{k}) - \epsilon_{j\sigma}(\mathbf{k})}, & \text{if } i = 3, 4, \end{cases}\quad (\text{A10})$$

and

$$\gamma_{i\mathbf{k}\sigma} = (-1)^{i+1} \begin{cases} \frac{A_{13\sigma}(\epsilon_{i\sigma}(\mathbf{k}))}{\epsilon_{1\sigma}(\mathbf{k}) - \epsilon_{2\sigma}(\mathbf{k})} \prod_{j=3,4} \frac{1}{\epsilon_{i\sigma}(\mathbf{k}) - \epsilon_{j\sigma}(\mathbf{k})}, & \text{if } i = 1, 2 \\ \frac{A_{13\sigma}(\epsilon_{i\sigma}(\mathbf{k}))}{\epsilon_{3\sigma}(\mathbf{k}) - \epsilon_{4\sigma}(\mathbf{k})} \prod_{j=1,2} \frac{1}{\epsilon_{i\sigma}(\mathbf{k}) - \epsilon_{j\sigma}(\mathbf{k})}, & \text{if } i = 3, 4. \end{cases}\quad (\text{A11})$$

By solving numerically the system of equations in Eqs. (A6), we get the important physical parameters in the system, such as the energy necessary for the single-quasiparticle excitations (creation or annihilation)  $\mu$ , the average charge density imbalance function  $\delta \bar{n}$ , which describes the dynamical changes of the average electron densities in the layers, and the excitonic order parameter  $\Delta_{\sigma}$  as well.

## APPENDIX B: HUBBARD-STRATANOVICH DECOUPLING OF THE NONLINEAR DENSITY TERMS

### 1. Decoupling of the Coulomb- $U$ term

Now we effectuate the HS transformation of the nonlinear density terms in the Hamiltonian in Eq. (1). The density operators in Eqs. (6), (8), and (9) are now given in terms of simple Grassmann complex variables, and we can write for the

product  $n_{\eta\uparrow}n_{\eta\downarrow}$  in the  $U$  term in Eq. (4) the following relation:

$$n_{\eta\uparrow}(\mathbf{r}\tau)n_{\eta\downarrow}(\mathbf{r}\tau) = \frac{1}{4}[n_{\eta}^2(\mathbf{r}\tau) - (\mathbf{n}_{\eta}(\mathbf{r}\tau)\hat{\sigma}_z)^2]. \quad (\text{B1})$$

The vector-operator  $\hat{\mathbf{n}}_{\eta}(\mathbf{r})$  in Eq. (B1) is a two-dimensional vector, given as

$$\hat{\mathbf{n}}_{\eta}(\mathbf{r}) = (\hat{n}_{\eta\uparrow}(\mathbf{r}), \hat{n}_{\eta\downarrow}(\mathbf{r})). \quad (\text{B2})$$

The product  $\mathbf{n}_{\eta}(\mathbf{r}\tau)\hat{\sigma}_z$  on the right-hand side of Eq. (B1) is indeed the charge-density difference between different spin configurations  $\sigma = \uparrow$  and  $\sigma = \downarrow$ , i.e.,

$$\mathbf{n}_{\eta}(\mathbf{r}\tau)\hat{\sigma}_z = n_{\eta\uparrow}(\mathbf{r}\tau) - n_{\eta\downarrow}(\mathbf{r}\tau). \quad (\text{B3})$$

Then, the HS transformation looks like

$$e^{-\frac{U}{4}\sum_{\mathbf{r}}\int_0^{\beta}d\tau n_{\eta}^2(\mathbf{r}\tau)} = \int [\mathcal{D}V_{\eta}]e^{-\sum_{\mathbf{r}}\int_0^{\beta}d\tau\left(\frac{V_{\eta}^2(\mathbf{r}\tau)}{U} - in_{\eta}(\mathbf{r}\tau)V_{\eta}(\mathbf{r}\tau)\right)}. \quad (\text{B4})$$

The integration on the right-hand side of Eq. (B4) is evaluated over the auxiliary complex field  $V_{\eta}(\mathbf{r}\tau)$ . We can calculate this integral by using the saddle-point approximation of it. Indeed, this procedure is equivalent, in some sense, to the usual mean-field approximation. Moreover, the procedure described here is more precise, since it deals with a more general form of the generating function. In the exponential on the right-hand side of Eq. (B4), we have a function  $f[V_{\eta}, n_{\eta}]$ , given as

$$f[V_{\eta}, n_{\eta}] = \sum_{\mathbf{r}} \int_0^{\beta} d\tau \left( -\frac{V_{\eta}^2(\mathbf{r}\tau)}{U} + in_{\eta}(\mathbf{r}\tau)V_{\eta}(\mathbf{r}\tau) \right), \quad (\text{B5})$$

and we approximate the integral as

$$\int [\mathcal{D}V_{\eta}]e^{f[V_{\eta}, n_{\eta}]} = e^{f[V_{0\eta}, n_{\eta}]}, \quad (\text{B6})$$

where  $V_{0\eta}$  is the saddle-point value of the variable  $V_{\eta}(\mathbf{r}\tau)$ . We calculate the saddle-point value by solving the equation

$$f'[V_{\eta}] = 0. \quad (\text{B7})$$

Then we get for  $V_{0\eta}$ :

$$V_{0\eta} = \frac{iU}{2}\langle n_{\eta} \rangle. \quad (\text{B8})$$

Here,  $\langle n_{\eta} \rangle$  is the grand canonical average of the density function  $n_{\eta}(\mathbf{r}\tau)$ . It could be calculated exactly with the help of the partition function in Eq. (12) as

$$\langle \dots \rangle = \frac{1}{\mathcal{Z}} \int \prod_{\eta} [\mathcal{D}\bar{\eta}\mathcal{D}\eta] \dots e^{-S}. \quad (\text{B9})$$

Next, the contribution to the action in Eq. (13), coming from the decoupling given in Eq. (B4) is

$$\mathcal{S}[V_{0\eta}] = -\sum_{\mathbf{r}} \int_0^{\beta} d\tau \frac{U}{2} \bar{n}_{\eta} n_{\eta}(\mathbf{r}\tau) \quad (\text{B10})$$

and the contribution to total Hamiltonian in Eq. (1) is

$$\Delta\mathcal{H}_U = \frac{U}{2} \sum_{\mathbf{r}} \bar{n}_{\eta} n_{\eta}(\mathbf{r}\tau). \quad (\text{B11})$$

The decoupling of the quadratic charge density difference term  $(U/4)\int_0^{\beta}d\tau\sum_{\mathbf{r}}(\hat{\mathbf{n}}_{\eta}(\mathbf{r}\tau)\hat{\sigma}_z)^2$  is also obvious:

$$e^{\frac{U}{4}\sum_{\mathbf{r}}\int_0^{\beta}d\tau(n_{\eta}(\mathbf{r}\tau)\hat{\sigma}_z)^2} = \int [\mathcal{D}\zeta]e^{-\sum_{\mathbf{r}}\int_0^{\beta}d\tau\left(\frac{\zeta_{\eta}^2(\mathbf{r}\tau)}{U} - \zeta_{\eta}(\mathbf{r}\tau)n_{\eta}(\mathbf{r}\tau)\hat{\sigma}_z\right)}. \quad (\text{B12})$$

Within the same saddle-point approximation procedure, we can calculate the average values of the decoupling field  $\zeta_{\eta}(\mathbf{r}\tau)$ . (Indeed, the average value obtained within this method is equivalent to the one calculated within the usual mean-field theory). We get

$$\zeta_{0\eta} = \frac{U}{2}\langle n_{\eta}(\mathbf{r}\tau)\hat{\sigma}_z \rangle. \quad (\text{B13})$$

Indeed, we suppose the equal average spin populations in the system at equilibrium, thus, we have  $\langle n_{\eta\uparrow}(\mathbf{r}\tau) \rangle = \langle n_{\eta\downarrow}(\mathbf{r}\tau) \rangle$ , therefore, we get  $\langle \mathbf{n}_{\eta}(\mathbf{r}\tau)\hat{\sigma}_z \rangle = 0$ . Thus, we put  $\zeta_{0\eta} = 0$ .

## 2. Decoupling of the Coulomb- $W$ term

A simple operator calculus shows that the interlayer Coulomb interaction term  $W$  can be rewritten in a more efficient form by using the auxiliary excitonic operators

$$\hat{\xi}_{\sigma\sigma'}^{(a)}(\mathbf{r}) = \hat{a}_{\sigma}^{\dagger}(\mathbf{r})\hat{a}_{\sigma'}(\mathbf{r}) \quad (\text{B14})$$

and

$$\hat{\xi}_{\sigma\sigma'}^{(b)}(\mathbf{r}) = \hat{b}_{\sigma'}^{\dagger}(\mathbf{r})\hat{b}_{\sigma}^{\dagger}(\mathbf{r}). \quad (\text{B15})$$

We can write

$$\mathcal{H}_W = 2W \sum_{\mathbf{r}} \sum_{\eta=a,b} \hat{n}_{\eta}(\mathbf{r}) - W \sum_{\mathbf{r}\sigma\sigma'\lambda} |\hat{\xi}_{\sigma\sigma'}^{(\lambda)}(\mathbf{r})|^2, \quad (\text{B16})$$

where  $\lambda = a, b$ , according to definitions in Eqs. (B14) and (B15). Then we can decouple the biquadratic fermionic term in Eq. (B16) by employing again the Grassmann-field path integration techniques and then the saddle-point approximation for the auxiliary fermionic fields  $\bar{\Delta}_{\sigma\sigma'}^{(\lambda)}(\mathbf{r}\tau)$  and  $\Delta_{\sigma\sigma'}^{(\lambda)}(\mathbf{r}\tau)$ , introduced above. The HS decoupling of the  $W$  term is

$$\begin{aligned} & \exp\left(W \sum_{\mathbf{r}} \sum_{\sigma\sigma'} \sum_{\lambda} \int_0^{\beta} d\tau |\xi_{\sigma\sigma'}^{(\lambda)}(\mathbf{r}\tau)|^2\right) \\ &= \int \prod_{\lambda} [\mathcal{D}\bar{\Delta}^{(\lambda)}\mathcal{D}\Delta^{(\lambda)}] e^{-\frac{1}{W}\sum_{\mathbf{r}}\sum_{\sigma\sigma'}\sum_{\lambda}\int_0^{\beta}d\tau|\Delta_{\sigma\sigma'}^{(\lambda)}(\mathbf{r}\tau)|^2} \\ & \quad \times e^{\sum_{\mathbf{r}}\sum_{\sigma\sigma'}\sum_{\lambda}\int_0^{\beta}d\tau(\bar{\Delta}_{\sigma\sigma'}^{(\lambda)}(\mathbf{r}\tau)\xi_{\sigma\sigma'}^{(\lambda)}(\mathbf{r}\tau) + \Delta_{\sigma\sigma'}^{(\lambda)}(\mathbf{r}\tau)\bar{\xi}_{\sigma\sigma'}^{(\lambda)}(\mathbf{r}\tau))}. \end{aligned} \quad (\text{B17})$$

Next, we consider the function in the exponential on the right-hand side of Eq. (B17) and we replace the integral by the saddle-point value of the exponential function at points  $\bar{\Delta}_{0\sigma\sigma'}^{(\lambda)}$  and  $\Delta_{0\sigma\sigma'}^{(\lambda)}$ . In turn, those saddle-point values could be obtained after functional derivation of the integral on the right-hand side of Eq. (B17) and we get the following values:

$$\begin{aligned} \Delta_{0\sigma\sigma'}^{(\lambda)} &= W\langle \xi_{\sigma\sigma'}^{(\lambda)}(\mathbf{r}\tau) \rangle, \\ \bar{\Delta}_{0\sigma\sigma'}^{(\lambda)} &= W\langle \bar{\xi}_{\sigma\sigma'}^{(\lambda)}(\mathbf{r}\tau) \rangle. \end{aligned} \quad (\text{B18})$$

Indeed, the parameters  $\Delta_{0\sigma\sigma'}^{(\lambda)}$  and  $\bar{\Delta}_{0\sigma\sigma'}^{(\lambda)}$  obtained above represent the mean-field values of the excitonic gap parameters  $\Delta_{\sigma\sigma'}^{(\lambda)}$  and  $\bar{\Delta}_{\sigma\sigma'}^{(\lambda)}$ , i.e.,

$$\begin{aligned}\Delta_{0\sigma\sigma'}^{(\lambda)} &= \Delta_{\sigma\sigma'}^{(\lambda)}, \\ \bar{\Delta}_{0\sigma\sigma'}^{(\lambda)} &= \bar{\Delta}_{\sigma\sigma'}^{(\lambda)}.\end{aligned}\quad (\text{B19})$$

Furthermore, we suppose them as real and we put  $\sigma = \sigma'$  (this corresponds to the case of pairing between electrons and holes with opposite spin directions). On the other hand, for the homogeneous AA-BLG system, we have  $\Delta_{\sigma\sigma'}^{(a)} = \Delta_{\sigma\sigma'}^{(b)}$  and we

can omit the sublattice index  $\lambda$ . Thus, we have

$$\bar{\Delta}_{\sigma\sigma'}^{(\lambda)} = \Delta_{\sigma\sigma'}^{(\lambda)} = \Delta_{\sigma}^{(\lambda)} \equiv \Delta_{\sigma}.\quad (\text{B20})$$

Then, the contribution to total Hamiltonian in Eq. (1) coming from the decoupling procedure will be

$$\Delta\mathcal{H}_W = - \sum_{\mathbf{r}\sigma} \sum_{\lambda} \Delta_{\sigma} \xi_{\sigma}^{(\lambda)}(\mathbf{r}).\quad (\text{B21})$$

It is interesting to remark at the end of this Appendix that the quadratic terms in  $\langle n_{\eta} \rangle$ ,  $\Delta_{0\eta\sigma\sigma'}$ , and  $\bar{\Delta}_{0\eta\sigma\sigma'}$ , appearing when putting back those saddle-point values in the respective functions in exponentials, give just the constant contributions to the total Hamiltonian of the system and, therefore, we neglect them for the first treatment.

- 
- [1] E. V. Castro, K. S. Novoselov, S. V. Morozov, N. M. R. Peres, J. M. B. Lopes dos Santos, J. Nilsson, F. Guinea, A. K. Geim, and A. H. Castro Neto, Biased Bilayer Graphene: Semiconductor with a Gap Tunable by the Electric Field Effect, *Phys. Rev. Lett.* **99**, 216802 (2007).
- [2] E. McCann and M. Koshino, The electronic properties of bilayer graphene, *Rep. Prog. Phys.* **76**, 056503 (2013).
- [3] A. V. Rozhkov, A. O. Sboychakov, A. L. Rakhmanov, and F. Nori, Electronic properties of graphene-based bilayer systems, *Phys. Rep.* **648**, 1 (2016).
- [4] Sh. Okano, A. Sharma, F. Ortmann, A. Nishimura, Ch. Günther, O. D. Gordan, K. Ikushima, V. Dzhegagan, G. Salvan, and D. R. T. Zahn, Voltage-controlled dielectric function of bilayer graphene, *Adv. Opt. Mater.* **8**, 2000861 (2020).
- [5] L. Yan, A. Zhi-Min, W. Tao, W. Wen-Bo, S. Kuang, and Y. Bin, Transformation from AA to AB-stacked bilayer graphene on  $\alpha$ -SiO<sub>2</sub> under an electric field, *Chin. Phys. Lett.* **28**, 087303 (2011).
- [6] K. Szałowski, Ferrimagnetic and antiferromagnetic phase in bilayer graphene nanoflake controlled with external electric fields, *Carbon* **118**, 78 (2017).
- [7] T. Wang, Q. Guo, Y. Liu, and K. Sheng, A comparative investigation of an AB- and AA-stacked bilayer graphene sheet under an applied electric field: A density functional theory study, *Chin. Phys. B* **21**, 067301 (2012).
- [8] J. Borysiuk, J. Sołtys, and J. Piechota, Stacking sequence dependence of graphene layers on SiC (000-1)-Experimental and theoretical investigation, *J. Appl. Phys.* **109**, 093523 (2011).
- [9] B. Huet and J.-P. Raskin, Role of Cu foil in-situ annealing in controlling the size and thickness of CVD graphene domains, *Carbon* **129**, 270 (2018).
- [10] H.-L. Liu, Y. Liu, T. Wang, and Z.-M. Ao, AA bilayer graphene on Si-terminated SiO<sub>2</sub> under electric field, *Chin. Phys. B* **23**, 026802 (2014).
- [11] H.-V. Roy, C. Kallinger, and K. Sattler, Study of single and multiple foldings of graphitic sheets, *Surf. Sci.* **407**, 1 (1998).
- [12] J.-K. Lee, S.-C. Lee, J.-P. Ahn, S.-C. Kim, J. I. B. Wilson, and P. John, The growth of aa graphite on (111) diamond, *J. Chem. Phys.* **129**, 234709 (2008).
- [13] C.-W. Chiu, S.-C. Chen, Y.-C. Huang, F.-L. Shyu, and M.-F. Lin, Critical optical properties of AA-stacked multilayer graphenes, *Appl. Phys. Lett.* **103**, 041907 (2013).
- [14] H. M. Abdullah, M. Al Ezzi, and H. Bahlouli, Electronic transport and Klein tunneling in gapped AA-stacked bilayer graphene, *J. Appl. Phys.* **124**, 204303 (2018).
- [15] W.-X. Wang, L.-J. Yin, J.-B. Qiao, T. Cai, S.-Y. Li, R.-F. Dou, J.-C. Nie, X. Wu, and L. He, Atomic resolution imaging of the two-component Dirac-Landau levels in a gapped graphene monolayer, *Phys. Rev. B* **92**, 165420 (2015).
- [16] J. Jung, A. M. DaSilva, A. H. MacDonald, and Sh. Adam, Origin of band gaps in graphene on hexagonal boron nitride, *Nat. Commun.* **6**, 6308 (2015).
- [17] M. Gmitra, S. Konschuh, C. Ertler, C. Ambrosch-Draxl, and J. Fabian, Band-structure topologies of graphene: Spin-orbit coupling effects from first principles, *Phys. Rev. B* **80**, 235431 (2009).
- [18] A. Dyrdał and J. Barnaś, Spin Hall effect in AA-stacked bilayer graphene, *Solid State Commun.* **188**, 27 (2014).
- [19] E. Prada, P. San-Jose, L. Brey, and H. A. Fertig, Band topology and the quantum spin Hall effect in bilayer graphene, *Solid State Commun.* **151**, 1075 (2011).
- [20] X. Zhai and G. Jin, Proposal for realizing the quantum spin Hall phase in a gapped graphene bilayer, *Phys. Rev. B* **93**, 205427 (2016).
- [21] A. O. Sboychakov, A. L. Rakhmanov, A. V. Rozhkov, and F. Nori, Metal-insulator transition and phase separation in doped AA-stacked graphene bilayer, *Phys. Rev. B* **87**, 121401(R) (2013).
- [22] T. Uchiyama, H. Goto, H. Akiyoshi, R. Eguchi, T. Nishikawa, H. Osada, and Y. Kubozono, Difference in gating and doping effects on the band gap in bilayer graphene, *Sci. Rep.* **7**, 11322 (2017).
- [23] R. S. Akzyanov, A. O. Sboychakov, A. V. Rozhkov, A. L. Rakhmanov, and F. Nori, AA-stacked bilayer graphene in an applied electric field: Tunable antiferromagnetism and coexisting exciton order parameter, *Phys. Rev. B* **90**, 155415 (2014).
- [24] V. Apinyan and T. K. Kopeć, Antiferromagnetic ordering and excitonic pairing in AA-stacked bilayer graphene, *Phys. Rev. B* **104**, 075426 (2021).
- [25] A. L. Rakhmanov, A. V. Rozhkov, A. O. Sboychakov, and F. Nori, Instabilities of the AA-Stacked Graphene Bilayer, *Phys. Rev. Lett.* **109**, 206801 (2012).
- [26] S. Sahu, S. K. Panda, and G. C. Rout, Tight-binding model study of the tunable anti-ferromagnetism and electron specific

- heat of AA-staked bi-layer graphene in a transverse electric field, *Mater. Today: Proc.* **9**, 438 (2019).
- [27] Y. Mohammadi, Tunable plasmon modes in doped AA-stacked bilayer graphene, *Superlattices Microstruct.* **156**, 106955 (2021).
- [28] A. Ahmet, V.-M. I. Jesus, T. J. You, K. G. K. Wai, W. Kenji, T. Takashi, A. Shaffique, and Ö. Barbaros, Electronic spin transport in dual-gated bilayer graphene, *NPG Asia Mater.* **8**, e274 (2016).
- [29] P. L. de Andres, R. Ramírez, and J. A. Vergés, Strong covalent bonding between two graphene layers, *Phys. Rev. B* **77**, 045403 (2008).
- [30] H. Rezanía and M. Abdi, Longitudinal magnetic field effects on thermal transport of doped bilayer graphene, *J. Supercond. Novel Magn.* **31**, 3995 (2018).
- [31] E. V. Kurganova, H. J. van Elferen, A. McCollam, L. A. Ponomarenko, K. S. Novoselov, A. Veligura, B. J. van Wees, J. C. Maan, and U. Zeitler, Spin splitting in graphene studied by means of tilted magnetic-field experiments, *Phys. Rev. B* **84**, 121407(R) (2011).
- [32] A. Belouad, Y. Zahidi, and A. Jellal, AA-stacked bilayer graphene quantum dots in magnetic field, *Mater. Res. Express* **3**, 055005 (2016).
- [33] A. Belouad and A. Jellal, Energy levels of magnetic quantum dots in gapped graphene, *Eur. Phys. J. B* **94**, 75 (2021).
- [34] S. Karimi and H. Rezanía, Effect of magnetic field on specific heat and magnetic susceptibility of biased bilayer graphene: A full band approach, *Chem. Phys.* **525**, 110417 (2019).
- [35] N. Kheirabadi, Electronic Properties of Bilayer Graphene in a Steady Magnetic Field, PhD. thesis, Lancaster University, 2018.
- [36] H. M. Abdullah, D. R. da Costa, H. Bahlouli, A. Chaves, F. M. Peeters, and B. Van Duppen, Electron collimation at van der Waals domain walls in bilayer graphene, *Phys. Rev. B* **100**, 045137 (2019).
- [37] B. D. Hoi and M. Yarmohammadi, Combined effect of the perpendicular magnetic field and dilute charged impurity on the electronic phase of bilayer AA-stacked hydrogenated graphene, *Phys. Lett. A* **382**, 3298 (2018).
- [38] M. F. C. Martins Quintela, J. C. C. Guerra, and S. M. Joao, Electronic properties of twisted bilayer graphene in the presence of a magnetic field, *EPJ Web Conf.* **233**, 03004 (2020).
- [39] R. Van Pottelberge, M. Zarenia, and F. M. Peeters, Magnetic field dependence of atomic collapse in bilayer graphene, *Phys. Rev. B* **98**, 115406 (2018).
- [40] J. Jia, P. K. Pyatkovskiy, E. V. Gorbar, and V. P. Gusynin, Broken symmetry states in bilayer graphene in electric and in-plane magnetic fields, *Phys. Rev. B* **95**, 045410 (2017).
- [41] Y. H. Kwan, S. A. Parameswaran, and S. L. Sondhi, Twisted bilayer graphene in a parallel magnetic field, *Phys. Rev. B* **101**, 205116 (2020).
- [42] V. Apinyan and T. K. Kopeć, Excitonic gap formation and condensation in the bilayer graphene structure, *Phys. Scr.* **91**, 095801 (2016).
- [43] K. Lee, B. Fallahzad, J. Xue, D. C. Dillen, K. Kim, T. Taniguchi, K. Watanabe, and E. Tutuc, Chemical potential and quantum Hall ferromagnetism in bilayer graphene, *Science* **345**, 58 (2014).
- [44] Y. Nam, D.-K. Ki, D. Soler-Delgado, and A. F. Morpurgo, Electron-hole collision limited transport in charge-neutral bilayer graphene, *Nat. Phys.* **13**, 1207 (2017).
- [45] G. Wagner, D. X. Nguyen, and S. H. Simon, Transport in Bilayer Graphene Near Charge Neutrality: Which Scattering Mechanisms are Important? *Phys. Rev. Lett.* **124**, 026601 (2020).
- [46] E. Brillaux, D. Carpentier, A. A. Fedorenko, and L. Savary, Nematic insulator at charge neutrality in twisted bilayer graphene, [arXiv:2008.05041](https://arxiv.org/abs/2008.05041).
- [47] Y. Da Liao, J. Kang, C. N. Breiø, X. Y. Xu, H.-Q. Wu, B. M. Andersen, R. M. Fernandes, and Z. Y. Meng, Correlation-Induced Insulating Topological Phases at Charge Neutrality in Twisted Bilayer Graphene, *Phys. Rev. X* **11**, 011014 (2021).
- [48] M. L. Cohen and J. R. Chelikowsky, *IV-VI Semiconductors* (Springer, Berlin, 1988), pp. 172–188.
- [49] H. Yu and J. F. Liu, Perfect spin-filtering in graphene monolayer-bilayer superlattice with zigzag boundaries, *Sci. Rep.* **6**, 25361 (2016).
- [50] L. Dell'Anna and A. De Martino, Wave-vector-dependent spin filtering and spin transport through magnetic barriers in graphene, *Phys. Rev. B* **80**, 155416 (2009).
- [51] M. Oltcher, F. Eberle, T. Kuczmik, A. Bayer, D. Schuh, D. Bougeard, M. Ciorga, and D. Weiss, Gate-tunable large magnetoresistance in an all-semiconductor spin valve device, *Nat. Commun.* **8**, 1807 (2017).
- [52] E. Hill, A. K. Geim, K. S. Novoselov, P. Blake, and F. Schedin, Graphene based spin valve devices, *IEEE Int. Magnet. Conf.*, 385 (2006).
- [53] S. Sahoo, T. Kontos, J. Furer, Ch. Hoffmann, M. Gräber, Au. Cottet, and Ch. Schönberger, Electric field control of spin transport, *Nat. Phys.* **1**, 99 (2005).
- [54] L. Huang, Y. Dai, J. Gao, P. Wang, R. Ding, and F. Wang, First-principles study on the threshold switch selector graphene/h-BN/graphene and the improvement of its performance, *Int. Conf. Electron. Circuits Inf. Eng.*, 6 (2021).
- [55] F. Volmer, M. Drögeler, G. Güntherodt, C. Stampfer, and B. Beschoten, Spin and charge transport in graphene-based spin transport devices with Co/MgO spin injection and spin detection electrodes, *Synth. Met.* **210**, 42 (2015).
- [56] F. Schwierz, Graphene electronics, in *Emerging Nanoelectronic*, edited by A. Chen, J. Hutchby, V. Zhirmov, and G. Bourianoff (John Wiley & Sons, Chichester, 2015), Chap. 15, p. 298.
- [57] L. Ma, Ph. X. Nguyen, Z. Wang, Y. Zeng, K. Watanabe, T. Taniguchi, A. H. MacDonald, K. F. Mak, and J. Shan, Strongly correlated excitonic insulator in atomic double layers, *Nature (London)* **598**, 585 (2021).
- [58] J. P. Eisenstein and A. H. MacDonald, Bose-Einstein condensation of excitons in bilayer electron systems, *Nature (London)* **432**, 691 (2004).
- [59] L. F. Register, X. Mou, D. Reddy, W. Jung, I. Sodemann, D. Pesin, A. Hassibi, A. H. MacDonald, and S. K. Banerjee, Bilayer pseudo-spin field effect transistor (BiSFET): Concepts and critical issues for realization, *ECS Trans.* **45**, 3 (2012).
- [60] M. Mucha-Kruczyński, E. McCann, and V. I. Falko, Electron-hole asymmetry and energy gaps in bilayer graphene, *Semicond. Sci. Technol.* **25**, 033001 (2010).
- [61] A. V. Volkov, A. A. Shylau, and I. V. Zozoulenko, Interaction-induced enhancement of  $g$  factor in graphene, *Phys. Rev. B* **86**, 155440 (2012).
- [62] L. D. Landau and E. M. Lifshitz, *Quantum Mechanics (Non-Relativistic Theory)*, 3rd ed. (Pergamon Press, Oxford, 1977).

- [63] J. W. Negele and H. Orland, *Quantum Many-Particle Systems* (Westview Press, Boulder, CO, 1998).
- [64] R. Phillips Feynman and A. R. Hibbs, *Quantum Mechanics and Path Integrals*, International Series in Pure and Applied Physics (McGraw-Hill, New York, NY, 1965).
- [65] A. A. Abrikosov, I. Dzyaloshinskii, L. P. Gorkov, and R. A. Silverman, *Methods of Quantum Field Theory in Statistical Physics* (Dover, New York, NY, 1975).
- [66] M. A. Alves and M. T. Thomaz, Berry's phase through the path integral formulation, *Am. J. Phys.* **75**, 552 (2007).
- [67] *Numerical Methods for Nonlinear Algebraic Equations*, edited by Ph. Rabinowitz (Gordon and Breach Science Publishers, London, 1970).
- [68] B. W. Adams, *Nonlinear Optics, Quantum Optics, and Ultrafast Phenomena with X-rays: Physics with X-ray Free-Electron Lasers* (Kluwer Academic Publishers, Boston, 2003).
- [69] V. A. Apinyan and T. K. Kopeć, Effective pairing interaction in the two-dimensional Hubbard model within a spin rotationally invariant approach, *Phys. Rev. B* **78**, 184511 (2008).